A framework for orbital performance evaluation in Distributed Space Missions for earth observation

A Framework for Orbital Performance Evaluation in Distributed Space Missions for Earth Observation

Sreeja Nag
Massachusetts Institute of Technology,
Cambridge, MA 02139
Email: sreeja_n@mit.edu

Jacqueline LeMoigne
NASA Goddard Space Flight Center (Software Engg. Div.)
Greenbelt, MD 20771
Jacqueline.LeMoigne@nasa.gov

David W. Miller
Massachusetts Institute of Technology & NASA HQ
Cambridge, MA 02139
Email: millerd@mit.edu

Olivier de Weck
Massachusetts Institute of Technology,
Cambridge, MA 02139
Email: deweck@mit.edu

Abstract— **Distributed Space Missions (DSMs) are gaining momentum in their application to earth science missions owing to their unique ability to increase observation sampling in angular, spatial, spectral and temporal dimensions simultaneously. DSM architectures have a large number of design variables and since they are expected to increase mission flexibility, scalability, evolvability and robustness, their design is a complex problem with many variables and objectives affecting performance. There are few open-access tools available to explore the tradespace of variables which allow performance assessment and are easy to plug into science goals, and therefore select the most optimal design. This paper presents a software framework developed on the MATLAB engine interfacing with STK, for DSM orbit design and selection. The associated tool is capable of generating thousands of homogeneous constellation or formation flight architectures based on pre-defined design variable ranges and sizing those architectures in terms of pre-defined performance metrics. The metrics can be input into observing system simulation experiments, as available from the science teams, allowing dynamic coupling of science and engineering designs. Design variables include constellation type, formation flight type, instrument view, altitude and inclination of chief orbits, differential orbital elements, leader satellites, latitudes or regions of interest, planes and satellite numbers. Intermediate performance metrics include angular coverage, number of accesses, revisit coverage, access deterioration over time at every point of the Earth's grid. The orbit design process can be streamlined and variables more bounded along the way, owing to the availability of low fidelity and low complexity models such as corrected HCW equations up to high precision STK models with J2 and drag. The tool can thus help any scientist or program manager select pre-Phase A, Pareto optimal DSM designs for a variety of science goals without having to delve into the details of the engineering design process. This paper uses cases measurements for multi-angular earth observation to demonstrate the applicability of the tool.**

TABLE OF CONTENTS

1. INTRODUCTION

Distributed Space Missions (DSMs) are gaining momentum in their application to Earth Observation (EO) missions owing to their unique ability to increase observation sampling in spatial, spectral, angular and temporal dimensions simultaneously. Spatial resolution of an image can be increased by using multiple satellites in formation flight to synthesise a long baseline aperture as shown for optical interferometry[1] and synthetic aperture radars. Constellations of evenly spaced satellites on repeat track orbits ensure temporal sampling within a few hours as well as continuous coverage maintenance. Spectral sampling can be improved by fractionating the payload (fractionated spacecraft) such that each physical entity images a different part of the spectrum and has customized optics to do so. Angular sampling or the ability to look at the same point on the ground at different angles (for reflectance studies or navigation) improves by flying many satellites in formation[2]. Since DSMs allow sampling improvement in any dimension by increasing number of satellites instead of individual sizes, radiometric resolution can be improved without compromising on other sampling requirements.

DSMs can be considered homogeneous or heterogeneous combinations of monolithic spacecraft. They include homogenous constellations like the Global Positioning System or heterogeneous ad-hoc flyers like the A-Train, autonomous formation flying clusters such as PRISMA and Edison (EDSN)[3], fractionated spacecraft such as the System F6 Program[4] and cellularized systems such as the DARPA Phoenix Program[5]. Formation flight, as required in clusters, fractionation or cellularization, entails active control of the individual spacecraft in order to maintain relative distances, orientations and geometry[6]. Fractionated spacecraft have the different spacecraft subsystems distributed over the physical entities and they exchange data, power and telemetry among each other. Cellularized systems are formed by assembling on-orbit resources called satlets to make aggregated, distributed systems. Since DSM architectures are defined by monolithic architecture variables and variables associated with the distributed framework, it leads to a large number of design

978-1-4799-5380-6/15/$31.00 ©2015 IEEE

variables. The number increases further in heterogeneous cases. DSMs are also expected to increase mission flexibility, scalability, evolvability and robustness as well as to minimize costs and risks associated with launch and operations. Thus, DSM design is a complex problem with many design variables, multiple objectives for performance, cost and emergent, often unexpected behavior.

.

2. DECISIONS IN DSM DESIGN

Designing space systems is not only technically challenging but also involves making hundreds of decisions early in the design cycle for allocating limited resources across the system and optimizing performance and cost. *EO performance* can be simplistically represented by spatial resolution, spatial range (swath, coverage), spectral resolution (wavelength bandwidth), spectral range (spectrum covered), angular resolution (number of view and solar illumination angles for the same image), angular range (spread of those angles), temporal range (mission lifetime), temporal resolution (repeat or revisit time), radiometric range (number of bits) and radiometric resolution (bits, signal to noise ratio).

Distributed systems have all the trades associated with monolithic systems *and* more associated with the network. Extra design variables include but are not restricted to the number of satellites and their individual masses, their orbits and inter-satellite spacing, existence and nature of inter-satellite communication and downlink schedules. These variables directly impact performance and cost. Performance variables, as defined, can be mutually conflicting across the spatial, spectral, temporal, angular and radiometric dimensions and within each dimension. For example, most earth observation satellites are placed in repeat ground track orbits so that the same point on the Earth is revisited regularly and frequently. Obviously, more frequent revisits imply that the rotation of the Earth and the orbit has to be adjusted in such a way that the satellite comes back to the same spot frequently, and as a result has less time to visit similar spots on other longitudes. Therefore, global spatial coverage or spatial range and temporal resolution are conflicting metrics. Both can be improved by increasing the swath of the satellite or the size of any instantaneous ground image. However, for a given number of pixels in an image, increasing its size or swath with increases the size of the pixels and coarsens resolution. Therefore, spatial range and temporal resolution are both conflicting metrics with respect to spatial resolution. Design variables need to be permuted to consider architectures that trade these metrics for an optimal design.

There are very few open-access tools available to explore the tradespace of variables, minimize cost and maximize performance for pre-defined science goals, and therefore select the most optimal design. This paper concentrates on a tool for computing angular performance metrics and their trade-offs with spatial and temporal performance. The spatial metrics obviously affect the spectral and radiometric performance, depending on the kind of spectrometer or radiometer used, which has been discussed in previous literature[7].

3. DISTRIBUTED SPACECRAFT FOR MULTI-ANGULAR OBSERVATION

Angular sampling implies taking images of the same ground spot at multiple 3D angles of solar incidence and reflection simultaneously. A near-simultaneous measurement requirement deems monolithic spacecraft insufficient for accurate and dense angular sampling[2][8]. Monolithic spacecraft have traditionally approximated the angular samples by combining measurements taken over time with forward-aft (e.g. TERRA's MISR[9]) or cross-track swath (e.g. TERRA's MODIS[10]) sensors. However, a single satellite can make measurements only along a restrictive plane with respect to the solar phase and most earth observation satellites are even more restricted since they are on sun-synchronous orbits. Further, the angular measurements are separated in time by many minutes along-track or weeks cross-track. In areas of fast changing surface/cloud conditions especially during the snow melt season/tropical storms, a few days can make a big difference in reflectance.

Near-simultaneous angular sampling can be improved by using a cluster or constellation of nanosatellites on a repeating-ground-track orbit[2],[8]. The cluster can make multi-spectral measurements of a ground spot at multiple 3D angles at the same time as they pass overhead either using narrow field of view (NFOV) instruments in controlled formation flight (Figure 1-a) or wide field of view (WFOV) instruments with overlapping ground spots providing integrated images at various angles (Figure 1-b). Parallel studies have demonstrated the technical feasibility of subsystems[11], suitability of payload development [7] to support such a mission, availability of science models to quantify the performance of such DSMs[2],[12],[13] as well as open-source flight software to continually update satellite capability for staged, scalable deployment[14], [15]. This paper focuses on generation of feasible formation flight and constellation architectures for all types of multi-angular measurements on the earth (Figure 1).

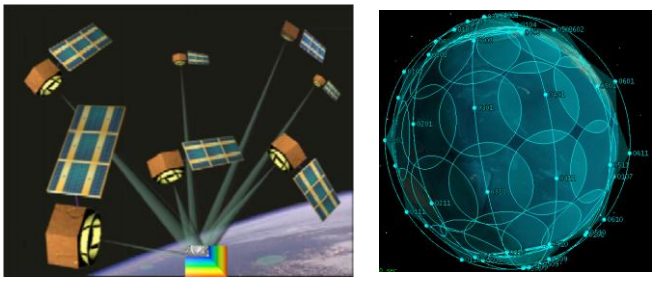

Figure 1: A DSM making multi-angular, multi-spectral measurements [Left] by virtue of pointing its NFOVs at the same ground spot, as it orbits the Earth as a single system (adapted from Leonardo BRDF[16]) or [Right] by virtue of their overlapping WFOVs over a large spread of angles.

Metrics for Angular Sampling

The widely accepted metric to quantify the angular dependence of remotely sensed signal is called BRDF or Bidirectional Reflectance-distribution function. BRDF of an optically thick body is a property of the surface material and its roughness. It is the ratio of reflected radiance to incident irradiance that depends on 3D geometry of incident and reflected elementary beams[17]. It depends on four major angles – the solar zenith (SZA) and azimuth angle (SAZ) and the view zenith (VZA) and azimuth angle (VAZ). The azimuth angles are simplified to one angle called the relative azimuth angle (RAZ). BRDF is used for the derivation of surface albedo[18], calculation of radiative forcing[19], land cover classification, cloud detection, atmospheric corrections, and aerosol optical properties [16].

Accurate BRDF time series at customized spectra and spatial scales can estimate many biophysical phenomena that are currently wrought with errors. For example, up to 90% of the errors in the computation of atmospheric radiative forcing, which is a key assessor of climate change, is attributed to the lack of good angular description of reflected solar flux and earth radiation budget (ERB)[20]. MODIS albedo retrievals show errors up to 15% due to its angular and spatial under-sampling when compared to CAR. Accuracy of BRDF estimation is therefore a representative metric of the 'goodness' of angular sampling.

Angular Trade-offs with Spatio-Temporal Sampling

Angular spread at the same ground spot affects spatial sampling which in turn affects temporal sampling. Increasing the boresight angle of view elongates the sensor footprint and coarsens spatial resolution[7]. Spatial resolution drops with greater angular spreads and thus look angles. This restricts the nadir resolution to a significantly small ground sample distance (GSD), to allow for resolution requirements for off-nadir pointing. Small GSD results in small swath, lower spatial coverage and less frequent revisits. Swath can be increased by adding more spatial pixels (and compromising on the spectral dimension[7]). Alternatively, swath can be kept the same and revisits increased by adding more clusters in the form of the clustellation. Each cluster would contribute to increasing angular spread while more clusters can improve spatial coverage and temporal revisits.

4. SOFTWARE TOOLS FOR ORBIT DESIGN

Computational tools for spacecraft and system design have been very important in making early design decisions. Model-based systems engineering is a focus of working groups under the International Council on Systems Engineering (INCOSE) and the developed tools have been applied to existing missions such as RAX[21] and PHOENIX[5]. Tools for space logistics and interplanetary transportation such as SpaceNET, modular and open source, are also available[22]. The CubeSat standard and associated documentation also provides a great resource to develop and integrate up to 3U (4 kg) spacecraft[23].

Existing Tools in Distributed Space Missions

Existing tools for monolithic spacecraft and other space design can be and have been adapted for distributed space systems. Individual components of space system design can be combined from different software. For example, orbit design can be done using NASA GSFC's GMAT (General Mission Analysis Tool) or NASA JSC's Copernicus tool. Spacecraft operations can be aided by NASA JPL's Activity Plan Generator (Automated Scheduling and Planning Environment (ASPEN) or Maestro tools. Specific interfaces for risk and science return for Saturn and Mars missions are also available. Tools for specific science data analysis such as USGS's Integrated Software for Imagers and Spectrometers (ISIS) and ESA's Rosetta Science Planning tool can be modified for some mission design. Cost/risk associated with distributed launches, staged deployment and reconfigurable constellations, all of which allow flexible design with increased costs, have been studied at MIT[24].

Need for a new Tool for Earth Observation

While all the above tools are great for specific missions and specific components, there is no off-the-shelf, modular tool for DSM design that can be used at the high-level architecture phase when key decisions are made. With the advent of hundreds of small satellites currently in orbit, and companies such as PlanetLabs and Skybox launching constellations in dozens, there is need for an integrated and modular tool which will enable easy plug into science metrics such as those for earth observation (extendable to astrophysics or navigation, etc.). Such a tool will allow rapid simulation of hundreds of architectures and their evaluation so that the "best" ones can be selected early in the design cycle. Since multi-angular earth observation has been established as an important field, we have developed such a tool for decisions related to DSM design for multiple angles.

5. RELEVANT FORMATION AND CONSTELLATION MODELS

Formation flight has been analyzed at several levels of fidelity, focusing on understanding and manipulating the relative motion of satellites in the Local Vertical Local Horizontal (LVLH) frame, for achieving large angular spread for any spot under the cluster. Constellations are analyzed in the global, Earth-centered and fixed frame (ECEF) for achieving large angular spread for any/all points on Earth within acceptable time spans.

Review of Formation Flight Models

The linearized Hill, Clohessy and Wiltshire equations, simplified to be known as the Hill's equations[25], [26] describe relative motion between any two spacecraft in a cluster, and can be extended to multiple spacecraft. In this framework, one satellite is assumed to be traveling in a circular Keplerian orbit while the others are perturbed from this orbit by a small quantity. The HCW Equations[25], [26] has the X axis pointing radially away from the earth and Y axis in the direction of motion, is given by:

$$a_x = \ddot{x} - 3n^2x - 2n\dot{y}$$
$$a_y = \ddot{y} + 2n\dot{x}$$
$$a_z = \ddot{z} + n^2z$$

(1)

The additional orbit perturbations over and above these accelerations are J2 effects due to non-spherical Earth (~2.4 X 10^{-6} m/s^2 in LEO), third body perturbations due to differential force by the Sun and Moon on the spacecraft (~3.6-4.3 X 10^{-5} m/s^2 in LEO), solar radiation pressure (~1.7X 10^{-10} m/s^2 in LEO) and atmospheric drag due to small differences in the spacecraft shape and ballistic coefficient and atmospheric properties (~3.2X 10^{-9} m/s^2 in LEO). The closed solutions to the Hill's equations i.e. relative geometries which do not need any active control to keep them intact have an analytical form with 6 initial conditions. The formations of interest within these forms are the string of pearls (SOP) where the satellites remain in a string in the along-track direction separated by a constant distance, say S km, cross track scan (CTS) which is the SOP configuration extended to include oscillations in the Z direction of any amplitude and phase desired and the free orbit ellipse (FOE) where all the satellites arranged in elliptical rings around the LVLH origin.

Since BRDF estimation requires VZA up to 80^o, very large inter-satellite distances are required which violate the assumptions of the HCW equations. HCW does not account for Earth's curvature and when propagated over a large time, the non-linear dynamics introduce large errors. Dual Spiral equations [27] provide relative equations of motion that analytically factor in Earth curvature. They represent the motion of a point about a secondary axis which in turn rotates about a primary axis. P($\Delta\alpha$,δ) represents the motion of the point in angles with respect to the primary axis, ρ_2 the angular radii of the point P from the secondary axis, (α_2,δ_2) the pole of the secondary axis with respect to the primary axis and ω, the rotation rate of the secondary axis.

$$\delta = 90 - a\cos\left[\sin\delta_2\cos\rho_2 + \cos\delta_2\sin\rho_2\cos\omega t\right]$$
$$\Delta\alpha = a\cos 2\left[\frac{\cos\rho_2 - \sin\delta_2\sin\delta}{\cos\delta_2\cos\delta}\right] \quad \textbf{(2)}$$

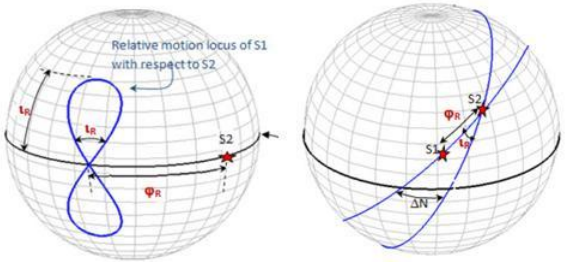

Figure 2: [Right] Two satellites in co-altitude circular orbits separated by relative inclination (i_R) and phase differences (ϕ_R). [Left] Relative motion of satellite 2 (S2) as seen from S1 (orbital plane marked by arrow) in an earth centered coordinate system, full sky geometry.

Under the assumption of the primary and secondary axis being mutually perpendicular at all times and ω representing the rotation of the Earth, the dual spiral equations reduce to the relative analemma equations which describes large-scale relative motion of co-altitude satellites in circular orbits using two key parameters are important, relative inclination (iR) i.e. the angle at which the orbits of the two satellites intersect, and the relative phase (φR) i.e. the angular separation between them when one passes through the others' place[27]. Relative inclination (iR) and relative phase (φR) are:

$$\cos i_R = \cos i_1\cos i_2 + \sin i_1\sin i_2\cos\Delta N$$
$$\Phi_R = (T_2 - T_1)n + \Delta\Phi$$

$$\Delta\Phi = \Phi_2 + \Phi_R - \Phi_1$$
$$\cos\Phi_1 = \frac{\cos i_2 - \cos i_1\cos i_R}{\sin i_R\sin i_2}$$
$$\cos\Phi_1 = \frac{\cos i_2 - \cos i_1\cos i_R}{\sin i_R\sin i_2} \quad \textbf{(3)}$$

Where ΔN is the angular separation along the equator of the two ascending nodes as shown in Figure 2a, T2-T1 is the time between the satellites crossing their respective ascending nodes, n is the angular motion of either satellite at their altitude and $\Delta\Phi$ is an intermediate variable (Figure 2) representing a difference in arc length from where the two orbits intersect to their respective ascending nodes. For circular co-altitude orbits, the relative motion of any satellite with respect to another is an analemma (figure-of-8) as seen in Figure 2-left. S2 is the base satellite and the analemma is the motion of S1 as seen by S2. Parametric equations for the analemma in the inertial earth-centric frame are given by the following form where α is the azimuth of S2 at the earth's center about the point where it crosses the orbital plane of S1 and δ is the elevation of S2 above the same point:

$$\sin\delta = \sin i_R\sin nt$$
$$\alpha = nt - \mathrm{atan}(\cos\mathrm{i_R}\tan\mathrm{nt}) \quad \textbf{(4)}$$

When the satellites are in the same orbital plane, the analemma reduces to a point offset from the base satellite by an amount equal to the spacing between the two satellites. The analemma trajectories indicate their usefulness for capturing both SOP and CTS configurations by including the curvature of the Earth analytically. For any pair of satellites separated in RAAN ($\Delta\Omega$) and true anomaly Δm, the maximum (λ_{max}) and minimum (λ_{min}) earth angle (λ) can be found from [28]:

$$\cos\lambda_{max} = cos^2(\Delta f/2)\cos\beta - sin^2(\Delta f/2)$$
$$\cos\lambda_{min} = cos^2(\Delta f/2) - sin^2(\Delta f/2)\cos\beta$$
$$\cos\beta = cos^2 i + sin^2 i\cos\Delta\Omega$$
$$\Delta f = \Delta m - 2tan^{-1}[-tan(\Delta\Omega/2)\cos i] \quad \textbf{(5)}$$

Higher fidelity models account for perturbations such as atmospheric drag, solar radiation pressure, non-spherical earth and third body effects that accumulate over several orbits and need to be corrected for periodically. The modified HCW equations introduce the effects of J2 perturbations due to the oblate shape of the Earth [29], and have an analytical form Equation (6) with parameters

described in [29]. When both J2 and atmospheric drag effects [30] are accounted for, the state matrix assumes a 7X7 form Equation (7), which is a modified version of the 6X6 dynamic state matrix, and is required to be solved numerically to compute relative satellite trajectories. Parameters in Equation (7) are described in [30].

$$x = x_0 Cos(\sqrt{1-s}\, nt) + \frac{\sqrt{1-s}}{2\sqrt{1+s}} y_0 Sin(\sqrt{1-s}\, nt)$$

$$y = -\frac{2\sqrt{1+s}}{\sqrt{1-s}} x_0 Sin(\sqrt{1-s}\, nt) + y_0 Cos(\sqrt{1-s}\, nt)$$

$$z = A(t)\left(\frac{z_0}{A(0)} Cos(B(t)\, t) + \frac{\left(\frac{\dot{z}_0}{n\sqrt{1+3s}}\right)}{A(0)} Sin(B(t)\, t) \right)$$

$$\dot{x}_0 = \frac{n\, y_0}{2} \frac{(1-s)}{\sqrt{1+s}} \qquad \dot{y}_0 = -2n\, x_0 \sqrt{1+s}$$

where

$$s = \frac{3 J_2 R_e^2}{8 r_{ref}^2} (1 + 3\, Cos\, 2 i_{ref})$$

$$A(t) = r_{ref} \Phi(t)$$

$$B(t) = n\sqrt{1+s} - \frac{\Delta\gamma}{t}$$

(6)

$$A = \begin{bmatrix} 0 & 0 & 0 & 1 & 0 & 0 & 0 \\ 0 & 0 & 0 & 0 & 1 & 0 & 0 \\ 0 & 0 & 0 & 0 & 0 & 1 & 0 \\ a41 & a42 & a43 & a44 & 0 & 0 & a47 \\ a51 & a52 & a53 & a54 & a55 & a56 & a57 \\ a61 & a62 & a63 & 0 & a65 & a66 & 0 \\ 0 & 0 & 0 & 0 & 0 & 0 & a77 \end{bmatrix}$$

where:

$$a41 = \omega_z^2 + 2\frac{\mu}{R^3} + K\left(1 - 3\sin^2 i \sin^2\theta\right)$$

$$a42 = \dot{\omega}_z + K\left(\sin^2 i \sin 2\theta\right) + \omega_z^2 \beta$$

$$a43 = -\omega_x \omega_z + K(\sin 2i \sin\theta)$$

$$a44 = -\beta\omega_z$$

$$a47 = \dot{r}$$

$$a51 = -\dot{\omega}_z + K\left(\sin^2 i \sin 2\theta\right) - \beta\omega_z^2$$

$$a52 = \omega_z^2 + \omega_x^2 - \frac{\mu}{R^3} + K\left[-\frac{1}{4} + \sin^2 i\left(\frac{7}{4}\sin^2\theta - \frac{1}{2}\right)\right]$$

$$a53 = \dot{\omega}_x + K\left(-\frac{1}{4}\sin 2i \cos\theta\right) + \beta\omega_x\omega_z$$

$$a54 = -2\omega_z$$

$$a55 = -\beta\omega_z$$

$$a56 = 2\omega_x$$

$$a57 = r\omega_z$$

$$a61 = -\omega_x\omega_z + K(\sin 2i \sin\theta)$$

$$a62 = -\dot{\omega}_x + K\left(-\frac{1}{4}\sin 2i \cos\theta\right) - \beta\omega_z\omega_x$$

$$a63 = \omega_x^2 - \frac{\mu}{R^3} + K\left[-\frac{3}{4} + \sin^2 i\left(\frac{5}{4}\sin^2\theta + \frac{1}{2}\right)\right]$$

$$a65 = -2\omega_x$$

$$a66 = -\beta\omega_z$$

$$a77 = -(\beta - \alpha)\omega_z$$

(7)

For the highest level of fidelity, orbit modeling and propagation software such as Analytical Graphics Inc. Systems Tool Kit's (AGI-STK[31]) High Precision Orbit Propagator (HPOP) is available. Full orbit propagation can be performed for all the satellites in the cluster and the solutions mapped into the LVLH frame with respect to a reference satellite. Closed cluster flight trajectories are formed when satellites are in orbits whose five Keplerian elements differ by a small amount or differentially. The relationships between the HCW coefficients in some simplified cases and the differential Keplerian elements is given by the COWPOKE equations or "Cluster Orbits with Perturbations of Keplerian Elements" [32]**.** The semi major axis is an exception because it corresponds to orbit energy, differing of which will break the formation. For circular LEO orbits, the HCW and differential Keplerian elements are related as:

$$x(t) = A_0 \cos(nt + \alpha) \qquad A_0 = -a\delta e$$

$$y(t) = -2A_0 \sin(nt + \alpha) + y_{off} \qquad B_0 = a\sqrt{\delta i^2 + \sin^2 i \delta\Omega^2}$$

$$z(t) = B_0 \cos(nt + \beta) \qquad \alpha = 0$$

$$\beta = \omega - \theta_z$$

$$y_{off} = a(\delta\omega + \delta M + \cos i \delta\Omega)$$

(8)

Review of Relevant Constellation Models

The utility of constellations for multi-angular observation is two-fold:

1. For global and/or more frequent coverage for NFOV payloads in formations as clustellations.
2. For global coverage for WFOV payloads as constellations, which thereby provides angular coverage.

Global, temporal sampling via constellations have been studied in the past [33] [34]. Only relevant literature to achieve multi-angle coverage will be focused here. WFOV constellations for MA-EO are most applicable to estimate the Earth's radiation budget (ERB). Sun-synchronous orbits are not good for this application because they miss the extreme of the systematic diurnal variations. Walker constellations have been studied recently [33][34] to be among the most efficient configurations for wide area continuous coverage. They rely on symmetric geometry and circular orbits to describe a constellation in only three variables corresponding to the number of planes, the number of satellites in each plane, and an inter-plane phasing parameter. Reference [28] and [35] has optimized Walker constellations to minimize global and regional revisit time respectively, and published the optimal number of planes, satellites and phasing for a given sensor field of view.

Continuous and complete global coverage is also provided by the Streets of Coverage pattern [36], with excess coverage at the poles [34]. Flower constellations [37], [38] provide a more generalized framework for relative orbits and coverage than Walker constellations. The flower satellites have identical altitude, inclination and eccentricity, like Walker, and are characterized by them as well as three additional integer parameters. The authors prove that they can project any symmetrical shape onto the Earth Centered Earth Fixed (ECEF) just by varying the defining parameters [39], can make it rotating frame independent and make the configuration compatible with J2 invariant orbits because altitude-inclination are free design variables. They have been applied theoretically to Earth Observation [40], among others such as communication and navigation. Recent work at MIT[41] has also shown the utility of ad-hoc constellations, put together entirely from secondary launches, is capable of generating acceptable global coverage.

6. PROPOSED FRAMEWORK FOR MULTI-ANGULAR TRADESPACE ANALYSIS

The framework to assess the optimal formation architectures (unique combination of design variables such as orbit parameters, payload FOV, imaging mode, etc.) and validate their BRDF estimation capabilities couples Model-Based Systems Engineering (MBSE) with Observing System Simulation Experiments (OSSE)[12]. A tradespace of formation architectures can be analyzed by varying the design variables in the MBSE model and assessing its effect on data assimilation and science products using OSSEs, as

shown in Figure 3. Only the constellation and formation flight architecture generation and preliminary evaluation will be discussed in this paper.

The systems engineering model for multi-angular applications has been enumerated in Figure 4 as an N2 diagram. Vertical arrows represent inputs into the modular subsystems (grey boxes) and horizontal arrows represent outputs. The model is iterative, as seen by the feedback loops and internal dependencies between subsystems. This paper concentrates only on orbits, or the first box. The outputs from the orbits module depend on if the DSM is a formation or constellation. The main output is angular sampling over time and temporal revisits (given an imaging mode for formations). The simplest imaging mode[13] for formation flight is assumed for this paper where a constant satellite is chosen as reference and looking nadir, while others point to the ground spot below the reference. Trades and design of the payload[7], subsystem capabilities to support such a mission[11], appropriate cost models[42] and coupling with appropriate OSSE models[2], [12], [13],[43] have been discussed in other literature.

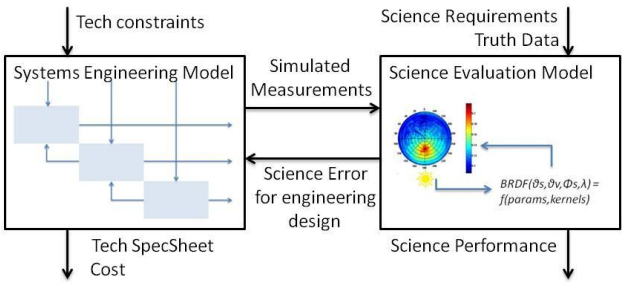

Figure 3: Summary of the overall approach to enumerate mission architectures under technical constraints and evaluate them based on proposed science products (right), tech specs and cost (left).

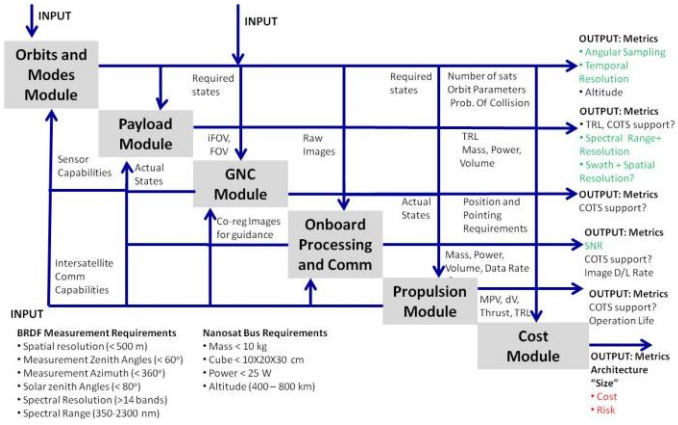

Figure 4: Systems Engineering Model (MBSE[11])

The science evaluation model[2],[13],[44] is based on complex BRDF models and validated against data collected by the airborne Cloud Absorption Radiometer (CAR) instrument, developed and operated by NASA Goddard Space Flight Center (GSFC) [16][20]. The CAR is designed to scan from zenith to nadir with a field of view (FOV) of 17.5 mrad and has 14 bands between 335 and 2344 nm. By flying the instrument around a particular ground spot in circles and at different heights it is possible to get thousands of multi-angular and multi-spectral radiance measurements used for the accurate estimation of BRDF [44] [45]. Figure 5 shows the land cover type distribution globally, as extracted from the NASA MODIS database. For each type, the angular reflectance as measured by CAR is shown as a polar plot where radius is the measurement zenith and azimuth, the relative azimuth angle with respect to the sun. The reflectance shown is at representative wavelengths: 1032 nm for snow, 432 nm for water, 682 nm for grasslands and forests, 870 nm for croplands, cities. The local angular dependence of reflectance is apparent and the goal of our mission is to characterize this dependence globally, not just by an oversimplified biome type and from scarce air data.

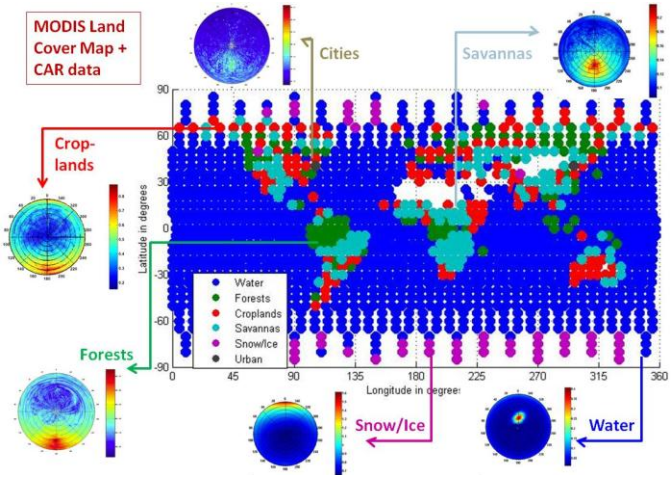

Figure 5: BRDF data[43] collected by the Cloud Absorption Radiometer during two NASA airborne campaigns.

The output metrics mentioned in this paper will feed into the science evaluation model and be used to decide the final orbits for the formation/constellation. The method has been published for albedo[13] or gross primary productivity[8] products using formations and ERB using constellations[12].

7. Implementing Distributed Orbits using the Proposed Framework

This section describes the modular implementation of the orbit generation module, both for formation flight and constellations. The architectures are enumerated to enable multi-angular earth observation so need large baselines (for NFOV angular spread) or multiple overlaps (for WFOV spread). The temporal trades are part of the WFOV angular trades because angular coverage per spot is achieved by satellite ground spot overlaps within an acceptable time. Figure 6 represents how constellations and their variables in the global, ECEF frame (left Box I) and/or formation flight geometries and their variables in the LVLH frame (right Box III) affect the angular and temporal performance

metrics in the center (Box II). The formation variables are not listed because they depend on the models listed (will be detailed in the next section). The metrics in Box II feed into the science evaluation or OSSE model. There are some formation imaging modes which use the constellation analysis software because they are optimized using performance at the ECEF ground spots (not in LVLH). The software's versatility to enable this demonstrated, but the application described elsewhere[13].

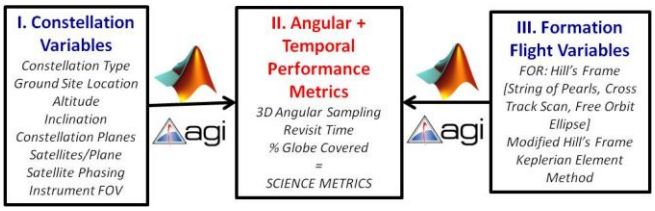

Figure 6: Process Flow Chart for tradespace analysis of DSMs with respect to constellation and formations.

Formation flight

Formation flight for multi-angular measurements (Figure 1-left) can be analyzed in a 3-layer framework of increasing model fidelity and decreasing computational ease of exploration - Figure 7. Each level's trades are analyzed in detail to streamline and inform the selection of variables in the next (higher fidelity) level. The final metrics are generated from MATLAB-controlled STK, however the streamlining exercise helps control the explosion of design variable combinations in a computationally expensive environment.

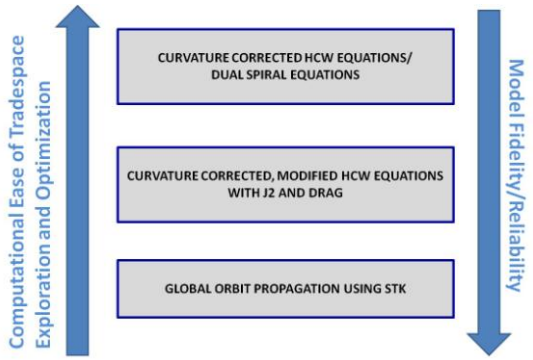

Figure 7: Levels of models used for formation flight simulation as a function of fidelity and computational ease of tradespace exploration.

All analysis in this section has been discussed in the Local Vertical Local Horizontal (LVLH) frame centered at the reference satellite at a 500 km altitude. The first level is the linearized Hill Clohessy Wiltshire Equations (1) which are numerically corrected to account for Earth's curvature at very large inter satellite distances by transforming from Cartesian to curvilinear coordinates. The HCW solution that gave the most angular diversity at the ground target was the Free Orbit Ellipse (FOE) configuration demonstrated in Figure 8 with 12 satellites + 1 looking nadir. The tradespace variables are the ring radius of the ellipses, their shape and their inclination with respect to the chief orbit. Figure 9 shows the trajectories (top) and the angles they subtend on the ground (bottom) when the initial x and z positions of the satellites are varied to give different orientations to the chief orbit. Relative azimuth and solar zenith angles are not plotted for simplicity. The red and green curves correspond to ellipses that project circles on the ground and are circles respectively. Since the trajectories represent the movement of each satellite over on orbit and the biome/ground spot below the cluster changes throughout, the mission designer can choose the optimal orientation based on the type of angular spread per biome they want. The COWPOKE equations say this implies tweaking the differential eccentricity, RAAN (Equation (8)).

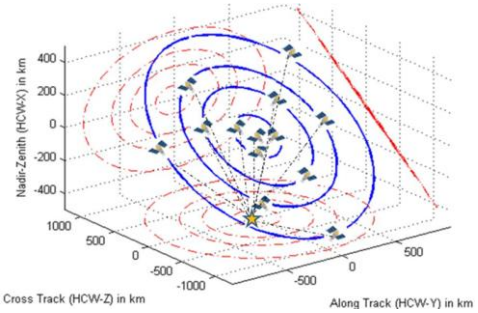

Figure 8: Free Orbit Ellipse simulated using the HCW equations with 12+1 satellites and numerically corrected for Earth curvature. Satellite trajectories are in LVLH and the orange star is at the origin's nadir.

The cross-track scan (CTS) and string of pearls (SOP) solutions were achieved using the dual spiral equations (Equation (2)) simplified into the relative analemma equations (Equation (3)). These solutions analytically accounts for the earth's curvature, azimuthal variation is not as easy to achieve as the FOE solution. The analemma equations can be customized for BRDF-related relative motion by transforming the parametric equations (4) from inertial earth centric coordinates to LVLH coordinates using the knowledge that the chief orbit is at a distance of (R_E+h) from the center of the earth, h being the orbital altitude and R_E, the radius of the earth. The transformation is given by:

$$x_k(t) = (\mathrm{R_E} + h)\left[\cos\big(\Phi_k + \alpha(t)\big)\sin\left(\frac{\pi}{2} - \delta(t)\right) - 1\right]$$
$$y_k(t) = (\mathrm{R_E} + h)\left[\sin\big(\Phi_k + \alpha(t)\big)\sin\left(\frac{\pi}{2} - \delta(t)\right)\right]$$
$$z_k(t) = (\mathrm{R_E} + h)\left[\cos\left(\frac{\pi}{2} - \delta(t)\right)\right] \quad \textbf{(9)}$$

Equation (9) represents the motion of the k'th satellite, located at a phase separation of Φ_k (= Φ_R in Figure 2) in the LVLH/HCW frame as seen by a base satellite that may be real or virtual, always located at the origin of the HCW frame. A 9 satellite and 1 reference satellite case in the CTS configuration (axes not equal) is shown in Figure 10– trajectories in blue and their projections on the perpendicular planes in red. The differential inclination and phases may be varied to get a large option of angular spreads over one orbit, as seen in Figure 11. The three curves toward the bottom correspond to those with negligible differential phase (middle trajectories in Figure

10). The six curves at the top of Figure 11 are the analemmas that flank the central one (analemma size increases with differential inclination). Maximum azimuthal coverage is obtained when the satellites go toward the extremes of the analemmas twice every orbit. Each satellite will have a unique analemma without any overlapping phase with another, to prevent collisions at the highest latitude, unlike FOE where multiple satellites can share an ellipse. Verifying with the COWPOKE equations Equation (8) for circular orbits, the only variable that can vary azimuthal spread, given phase, is differential inclination.

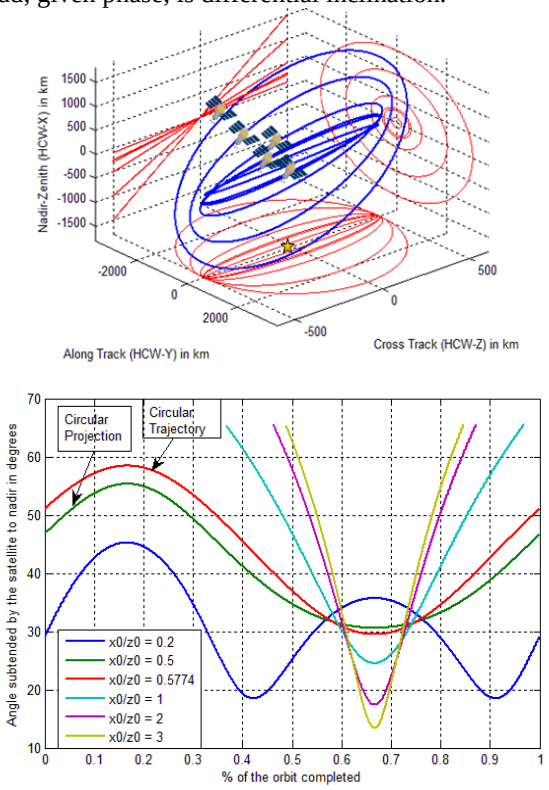

Figure 9: [Top] Curvature corrected FOE trajectories in LVLH frame for changing ellipse inclinations to chief orbit (x0/z0 ratio); [Bottom] View zenith angle subtended by a satellite at the ground spot directly below the LVLH origin for the FOE configurations shown.

The SOP configuration provides the same angular coverage as a monolithic satellite with many forward aft sensors (e.g. MISR) and provides limited azimuthal coverage, hence has not been explored in much detail. It can be simulated using the analemma equations but with no differential inclination.

Since the HCW and dual spiral level of analysis does not account for perturbations, the trajectories for every orbit are exactly the same. The second level of analysis introduces the effects of J2 perturbations due to the oblate shape of the Earth [29](Equation (6)) and then atmospheric drag effects [30]. Figure 12 shows the trajectories of 3 satellites in different colors with different ring sizes, simulated by maximum X-intercepts (Equation (7)). The orange star is the ground target directly below the reference satellite (marked). Initial X and Z positions and velocities can be varied in keeping with the HCW equations to get a large tradespace of trajectories corresponding to the HCW variables of ring sizes, shapes and orientations.

The expected tumbling effect of free-orbit ellipses about the cross track axis due to J2 effects is clearly seen in Figure 12. Additionally, there is a slight drift in the along-track direction due to atmospheric drag (negligible at 500 km altitude). The corresponding view zenith angles for all three rings, simulated at three different orientations, are seen in Figure 13. More the initial X position, larger the ellipse and more the angle subtended at nadir, as expected. The ellipses that make a 45deg or higher angle with the LVLH horizontal display two crests per orbit. The crests correspond to the two extreme positions in the along-track direction. They are symmetric at the beginning and lopsided after a day due to J2 tumbling in that direction. The zenith angle minima corresponds to the higher altitude side of the ellipse and the trough between the crests the lower altitude side. As the initial X-Z position ratios are varied to increase the inclination angle of the ellipse, the double crests become single because the ellipse tends toward a horizontal circle.

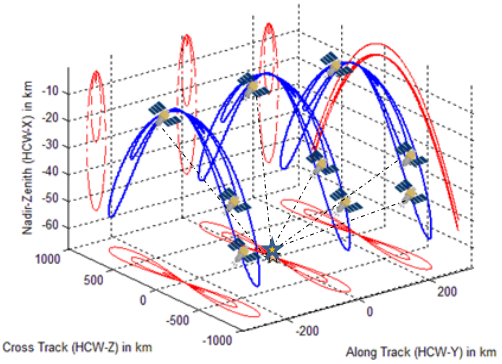

Figure 10: Cross Track Scan (CTS) simulated with 9+1 satellites with differential inclination and phase using the relative analemma model. Satellite trajectories are in LVLH and the orange star is at the origin's nadir.

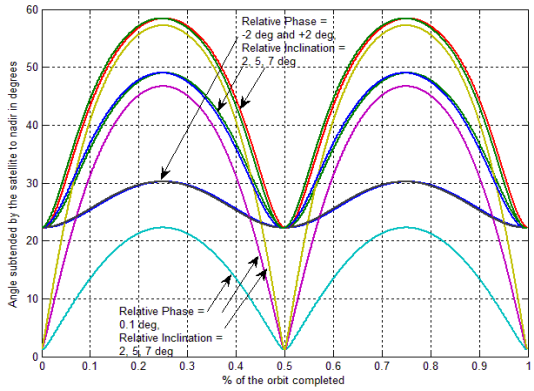

Figure 11: Variation of the view zenith angle subtended by a satellite at the ground target directly below the LVLH origin for the 9 satellites in Figure 10.

In terms of the angular output, lower inclinations are useful when a large variation of view zenith angle is needed over the orbit, for example, to follow the variation of the solar

zenith angle and precisely estimation specular reflection or hotspots. Higher inclinations are useful when an approximately constant view zenith is desired. Note that the relative azimuth with respect to the sun will show the same variation for all ellipses, because they share the same plane.

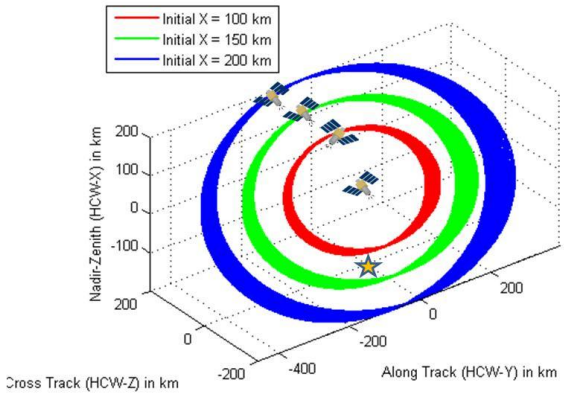

Figure 12: Free Orbit Ellipse with 3+1 satellites, simulated using the modified HCW equations with J2 and drag Equation (7) with appropriate initial conditions), propagated for 1 day. The satellite trajectories are in LVLH and the orange star represents the LVLH reference nadir.

To introduce azimuthal variation, an eccentric chief orbit is required with differential Keplerian[32]. The corresponding equations (also COWPOKE) are more complex than (8 and have not been analyzed in this paper. Parallel literature[11], [13] has shown that slightly eccentric orbits are beneficial in compensating for the drift in the along track direction and aid in keeping the formation together after 7-8 months of operation. It would be valuable to find the optimal chief and differential eccentricity that would allow a good azimuthal spread via free orbit ellipses as well as be beneficial to maintain. This analysis has been assigned to future work, alongside determining optimal chief orbits for the formations discussed in this paper. The 7X7 state transition matrix can be initialized with a finite Y and Z position, in order to simulate cross track scans that account for J2 and drag effects. As before, a constant atmospheric density of 0.02 kg/m^2, and a 6U CubeSat form factor for the satellites was assumed. Figure 14 shows 3+1 simulated trajectories, propagated for 1 day, where the reference satellite is at (0,0,0), directly above the orange star. The pattern corresponds exactly to Figure 10, except plotted on equal axes to differential between the extent of radial and along track drift due to drag and J2. The latter is far more, however it does not affect the formation because the relative spatial and angular spread between the satellites does not change much in a day. Global simulations using STK will show how these drifts are hugely affected by the differential Keplerian elements used to achieve the initial conditions.

The third and last framework of models uses AGI's Satellite Tool Kit to initialize and propagate individual satellite orbits (High Precision Orbital Propagator or HPOP) and then calculates their relative trajectories with respect to a reference satellite. SOP, CTS and FOE configurations of varying shapes, sizes and orientations can be created by varying the differential Keplerian elements of the satellite orbits. For example, verified by COWPOKE[32], when multiple satellites have the same Keplerian elements except separated by a small, differential true anomaly or TA, the resultant relative motion is the string of pearls (SOP). When multiple satellites have the same Keplerian elements except separated by a small, differential TA *as well as* inclination or RAAN, the resultant relative motion is the cross track scan (CTS). Finally, if satellites have different TA, inclination or RAAN *as well as* perigee or eccentricity, the resultant relative motion is the free orbit ellipse (FOE).

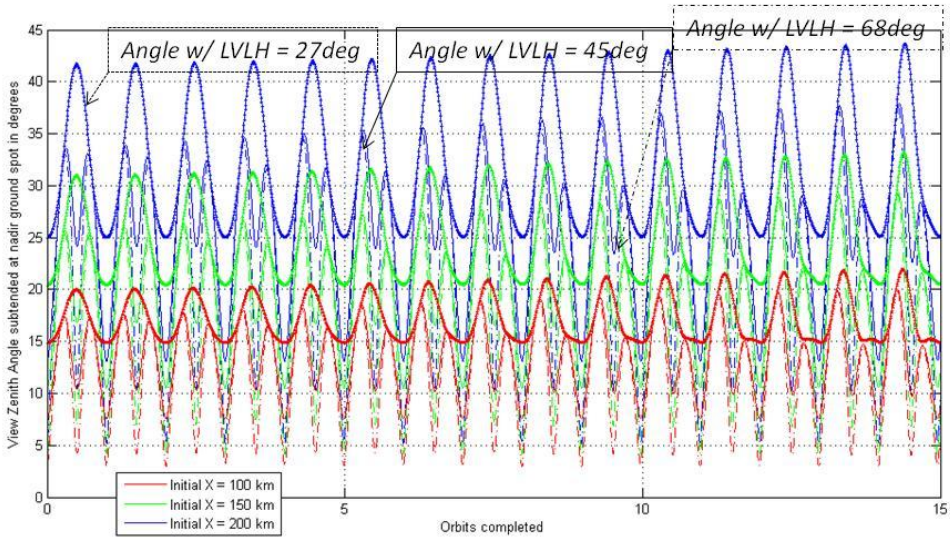

Figure 13: View zenith angle subtended at the ground target directly below the LVLH origin for the 3 satellite trajectories in Figure 12 (corresponding colors). The different line types correspond to different inclinations of the FOE with the LVLH horizontal plane containing the chief orbit (only one in Figure 12

External constraints like biome and latitude of interest determine the range of some variables for the angular trades. For example, differential inclination (RAAN) produces maximum separation at the poles (equator). FOE and CTS should be created by either one depending on target latitude where maximum angular spread is desired.

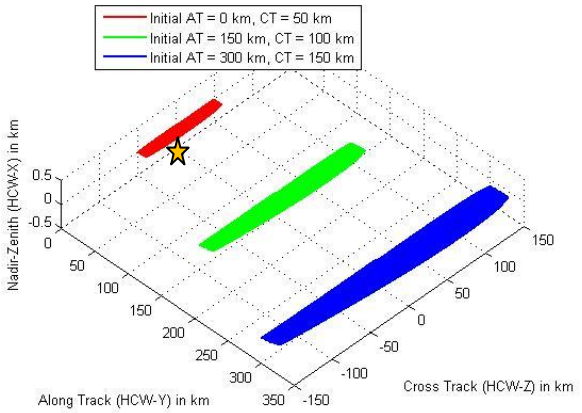

Figure 14: Cross track scan with 3+1 satellites, simulated using the modified HCW equations with J2 and drag Equation (7) with appropriate initial conditions), propagated for 1 day. The satellite trajectories are in LVLH and the orange star represents the LVLH reference nadir

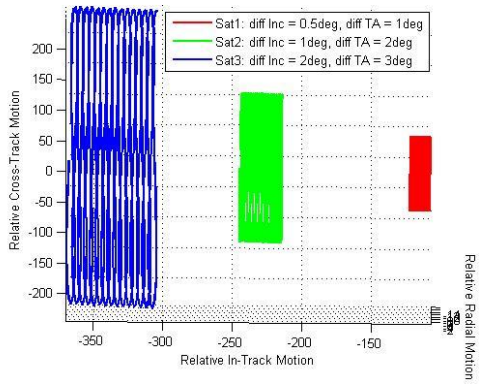

Figure 15: Cross track scan with 3+1 satellites, simulated on STK using differential TA and inclination, propagated for 1 day and satellite trajectories exported and plotted in the LVLH frame. The orange star represents the LVLH reference nadir.

Figure 15 shows the trajectories of 3+1 satellites with differential inclinations and TA, propagated on STK for 1 day. The drift associated with the formation to achieve hundreds of kilometers of baseline and angular spread (like Figure 10) is significant. Different inclinations cause the J2 forces on each satellite to be different causing the RAAN to rotate differently. A 20 deg view zenith angle spread takes less than 3 months to break up[11] because increasing RAAN differential causes the angular spread at the poles to decrease and equator to increase and eventually the latter is too large for the satellites to see each other. Figure 15 shows a drift not only in the along-track direction (as seen in Figure 14) but also in the radial direction, indicative of the formation breaking (similar to semi major axis difference).

When free orbit ellipses are simulated on STK using differential inclination, with TA and eccentricity, propagated for a day and plotted in the LVLH frame, a significant along track drift and tumbling effect is seen - Figure 16. This observation can be attributed to increasing RAAN spread due to the very different inclinations required to achieve the large baselines. The full extent of this drift is not seen in the modified HCW level of analysis. The loss of symmetry in the two-crests-per-orbit pattern for VZA is much faster in this model (Figure 17) than Figure 13. This is because there is no way to distinguish between LVLH–Z (cross track) due to inclination vs. RAAN. In reality, both have significant contribution, as is apparent from the COWPOKE equation for B_0 (Equation (8)), and can be used for design. The modified HCW analysis is thus used as an informative step in streamlining the maximum prescribed baseline for maintainable clusters, but the exact numbers and the ways to achieve those baselines are not relied upon.

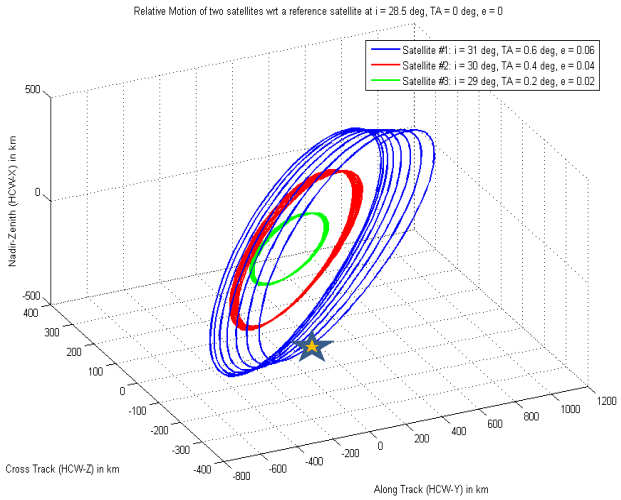

Figure 16: Free orbit ellipse with 3+1 satellites, simulated on STK using differential RAAN, TA and inclination, propagated for 1 day and satellite trajectories exported and plotted in the LVLH frame. The orange star represents the LVLH reference nadir.

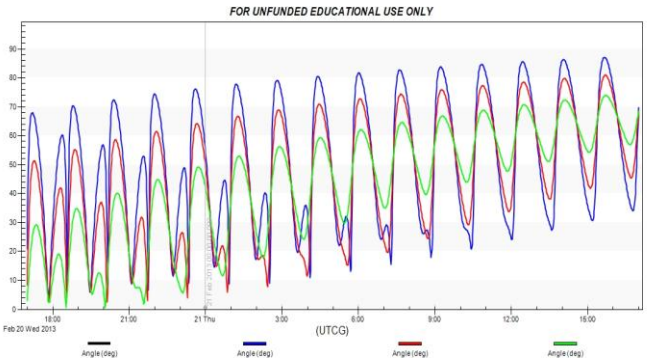

Figure 17: View zenith angle subtended at the ground target directly below the LVLH origin for the 3+1 satellite trajectories in Figure 16.

As indicated by the COWPOKE equation for B_0 (Equation (8)), cross track scans can be simulated using differential RAAN and TA. 3+1 satellites were propagated for 1 day on STK and the relative trajectories plotted in Figure 18. It is immediately apparent that compared to Figure 15, the drift in all directions is far less even with hundreds of kilometers of baseline and hence great angular spread on the ground. When the free orbit ellipse is simulated using differential RAAN instead of inclination, similar improvement in drift is seen (Figure 19). Some tumbling effect is seen as expected, in keeping with Figure 12. Going forward, only differential RAAN and TA (up to 6 deg) will be used to achieve formation spreads. 6 deg shows manageable drift, and sufficient angular spread, as will be shown in the next section. Since such formations will provide no azimuthal spread at the poles, different imaging modes (strategies to point the payload) will be used to achieve angular coverage at the poles, as described in other literature[13].

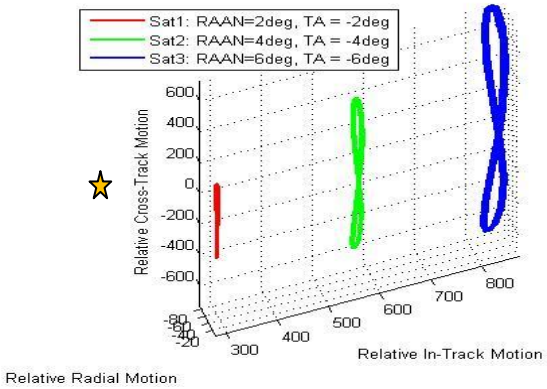

Figure 18: Cross track scan with 3+1 satellites, simulated on STK using differential RAAN and TA, propagated for 1 day and satellite trajectories exported and plotted in the LVLH frame. The orange star represents the LVLH reference nadir.

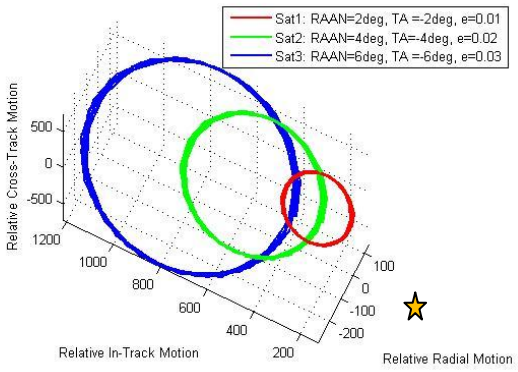

Figure 19: Free orbit ellipse with 3+1 satellites, simulated on STK using differential RAAN, TA and eccentricity, propagated for 1 day and satellite trajectories exported and plotted in the LVLH frame. The orange star represents the LVLH reference nadir.

BRDF has three major angles of interest, as mentioned before. Only view zenith angles have been shown in the paper so far. Solar zenith angles for the cluster and the relative azimuth angle with respect to the sun for every satellite in the cluster have been analyzed but not presented for brevity. It is important to note that those angles are equally important, and all three angles, i.e. 2N+1 angles for an N-satellite cluster per instant of time, serve as outputs from the orbits module and inputs into the science evaluation module driven by OSSEs. To demonstrate angular spread in the global frame, three candidate clusters with 9 satellites each (to match MISR's sensor numbers) were simulated in STK to image a specific spot on earth [0, -103.729] at a repeat period of 16 days and compared to the measurement spread of the same ground spot by MISR. Unlike 9 free-flyers, MISR has 9 cameras, one looking nadir and 4 each looking forward and aft at viewing angles of 26.1 deg, 45.6 deg, 60.0 deg and 70.5 deg. It can obtain 9 angular measurements on any ground spot in 10 minutes and its relative azimuth with respect to the sun at any given time is obtained from TERRA's TLE database within AGI STK. The overall arrangement is seen in Figure 20-top. One of the three clusters was in the SOP configuration (black) where in all Keplerian elements except the true anomaly were the same. The two other clusters were in different FOE configurations (blue and green), simulated by perturbing differential RAAN, eccentricity and TA only.

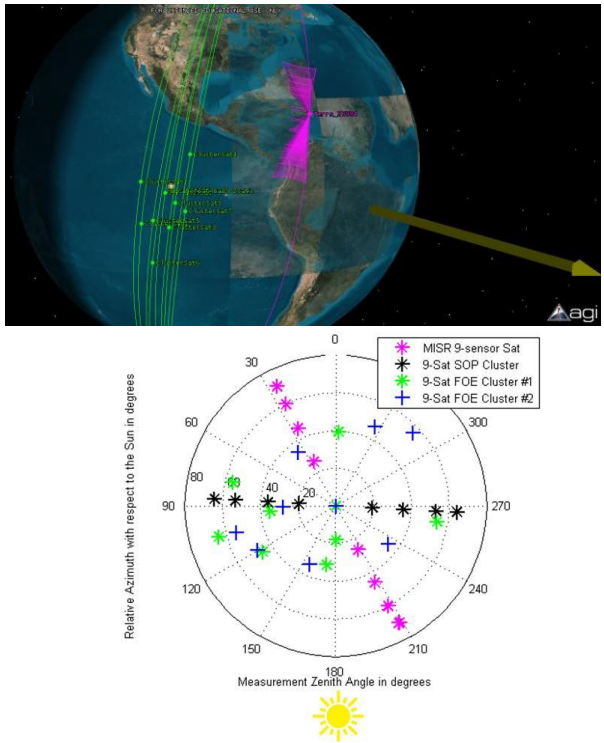

Figure 20: [Top] Global simulation of clusters (green dots as different architectures) vs. the MISR instrument with its 9 sensors (pink) [Bottom] BRDF polar plot for simulated measurements made by three 9-satellite clusters in SOP (black) and 2 different FOE configurations (green, blue) and the MISR instrument using 9 sensors (pink) of the same geographic location shown in (a). STK was used to calculate the instantaneous view zenith (radius) and view relative azimuth (azimuth) angles. The solar zenith angle is ~89°

There was an approximate 60° RAAN differential between the chief orbit of MISR and any of the clusters. Due to MISR's large swath, it has a total of ~1800s of access to the ground spot while the clusters have only 1.4s in 16 days.

The simulated angular measurements of the target are plotted on a BRDF polar plot for the time instant when the reference satellite is directly overhead the target - in Figure 20-bottom. The radius shows the view zenith angle and the polar azimuth the relative azimuth angle with respect to the sun, for a constant solar zenith. Since MISR has fixed sensors, the measurement zenith angles for a direct overpass (pink asterisks in Figure 20-bottom) are pre-determined and the relative solar azimuth is the angle between the velocity and sun vector measured in the satellite HCW X=0 plane. These measurements for a single overpass can be easily replicated by an SOP cluster (black asterisks in Figure 20-bottom). Improvement in angular performance is clearly demonstrated in both the FOE clusters because a large and diverse azimuthal and zenith spread on the BRDF plot is possible. Different architectures of different combinations of number of satellites and their differential Keplerian elements output such a spread at every instant of time, and these angular-temporal spreads serve as inputs to be evaluated in terms of how well they capture the 'true' BRDF in Figure 5[2], [13].

MATLAB-based software has been developed to automate formation architecture generation on AGI's STK, angular report creation for each architecture and angular metric calculation as a post-processing step, with the option to evaluate as is or pass into a science evaluation model. Architectures are generated by permuting allowable combinations of design variables – number of satellites, chief orbit altitude, inclination and differential RAAN and TA and the reference satellite among them.

Table 1: RAAN-TA (in deg) slots for the full factorial enumeration of formation architectures

RAAN	0	-5	5	0	-5	5	5	-5
TA	-5	-6	-4	5	6	4	-1	1

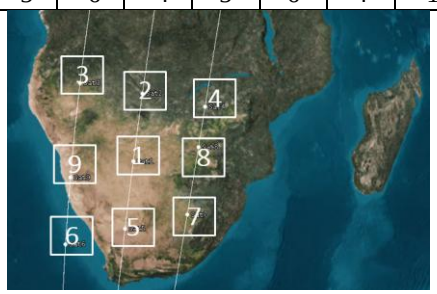

Figure 21: Eight available differential RAAN-TA slots (exact values in Table 1) arranged around the reference satellite (+1), as enumerated in an AGI-STK simulation.

To prevent variable space explosion and in keeping with the previous streamlining analysis, the number of satellites is limited between 3 and 8. Three satellites is the minimum required for the BRDF OSSE models and eight corresponds to NASA ARC's Edison Demonstration[3], currently the highest number of commissioned satellites in any DSM. Since studies[11][46] have shown that the only differential Keplerian elements maintainable using small sat technology are RAAN and TA, only they will be considered LVLH variables. For any given number of satellites (say, N), N-1 RAAN-TA differential combinations are picked from the 8 available (${}^{8}C_{N-1}$) in Table 1. These 8 slots have been selected as the corners of an approximate +/-5 deg square in RAAN and TA, with the reference satellite in the center and no common TAs to avoid collisions, as shown in Figure 21. Thus for a given altitude-inclination combination, there are a total of 1254 RAAN-TA combinations for 3 to 8 satellites.

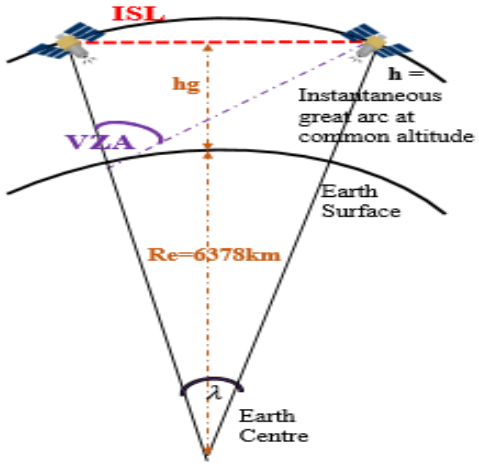

Figure 22: Representation of the geometry used to calculate view zenith angle (VZA) and inter-satellite link (ISL) between two spacecraft at altitude h.

The VZA subtended at the ground for a given RAAN-TA spread will differ by orbit altitude, as demonstrated in Figure 22. The same spread obviously results in lower VZA for higher altitudes so a larger spread is required to maintain the same VZA. Instantaneous VZA is calculated as the angle subtended under one satellite by another, λ is the angle subtended at the Earth center by both satellites and ISL (inter-satellite link) is the straight line distance between them. From geometry and the trigonometric sine law, VZA, h and ISL are found to be related as:

$$\sin x \cot VZA + cos\, x = h/ISL$$
$$ISL * \sin x = (Re + h) * \sin \lambda$$
$$ISL = 2 * \tan \lambda/2 \quad \textbf{(10)}$$

If the satellites in question are not in the same orbit, the great arc joining them at their common altitude is used for the calculations. Relative azimuth angle (RAZ) with respect to the sun will be calculated depending on the instantaneous orientation of this great arc plane with respect to the Sun. For a given altitude and inclination, the maximum VZA per orbit can be calculated from Equation (5) and (10). The trade-off between required differential RAAN and TA for two popular secondary launch orbits is shown in Figure 23. The bounds are chosen for the maximum RAAN-TA differential between any two satellites in Table 1's slots and the crosses indicate the differential of all those slots with

respect to a satellite at zero RAAN and TA (marked '1' in Figure 21). Charts for minimum VZA look the same, however are 2 deg lower.

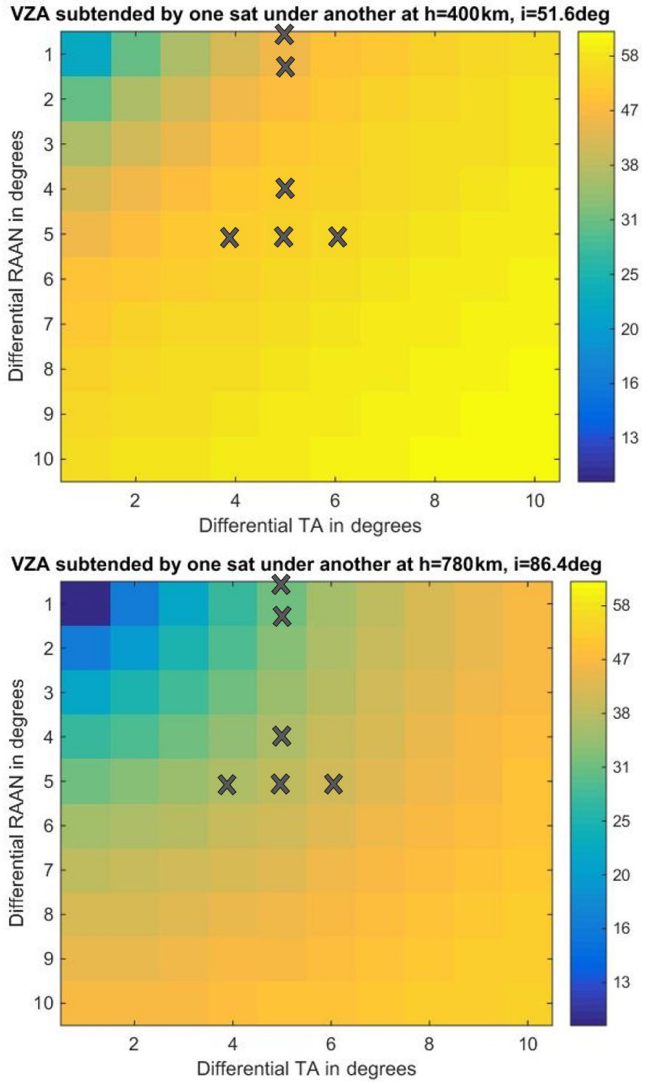

Figure 23: Dependence of maximum VZA subtended by one satellite under another as a function of their differential RAAN and TA, for secondary launches in the ISS (top) and Landsat orbit (bottom). Crosses mark the differential RAAN-TA of all 8 slots in Table 1 with respect to a satellite at RAAN=0, TA=0.

It is obvious from the figures that the crosses, or the same RAAN-TA spread, cluster around VZA ~ 50 deg for the ISS orbit but VZA ~ 35 deg for the LandSat orbit. Therefore for a fair comparison across chief orbit variables, the RAAN-TA spreads in Table 1 are scaled such that they average a maximum VZA of 45 deg at the ground spot below Sat #1 in Figure 22. Very precise differential RAAN-TA are not required because observing system simulations within the science evaluation model have shown that, given current models, a full RAZ spread and up to 45 deg of VZA improves science error to saturation[13],[47]. More importantly, orbit maintenance within arc-seconds of control is very expensive or impossible within CubeSat technologies[11]. Figure 24 captures the software process flow. MATLAB-driven STK generates customized reports (some listed in the middle column of Figure 24) which are named in keeping with the design variables for easy post-processing. The ones in red boxes contain the measurement zenith and relative azimuth with respect to the satellite's momentum vector, correspond to a 650 km altitude, 4 satellites, RAAN-TA combination #1 and the reference sat number (the one that looks nadir). Each report (.csv) contains view (zenith or azimuth or solar with respect to 2 perpendicular axes) angles of every satellite with respect to the reference. These reports are post-processed to output the 3 angles of interest (VZA, SZA, and RAZ) at every instant of time in the LVLH frame.

Constellations

When the DSM being analyzed is constellations, the analytical framework illustrated on the left side of Figure 6 is used. Spatial coverage and sampling in the global ECEF frame, not the LVLH frame, are orbital outputs when given inputs from the payload module (for pixel sizes and spectrometer type). Parameters such as the grid size on the earth (default: 5degX5deg in both latitude and longitude) and time sampling (default: 1 minute) can be defined. Using these requirements, automatic scripts on MATLAB drive STK to generate multiple architectures on STK by permuting the orbit design variables. For example, three architectures are pictured in Figure 25's left column. MATLAB-driven STK then commands each architecture definition to generate a full access report as a .cvaa file, some of which are seen in Figure 25's second column.

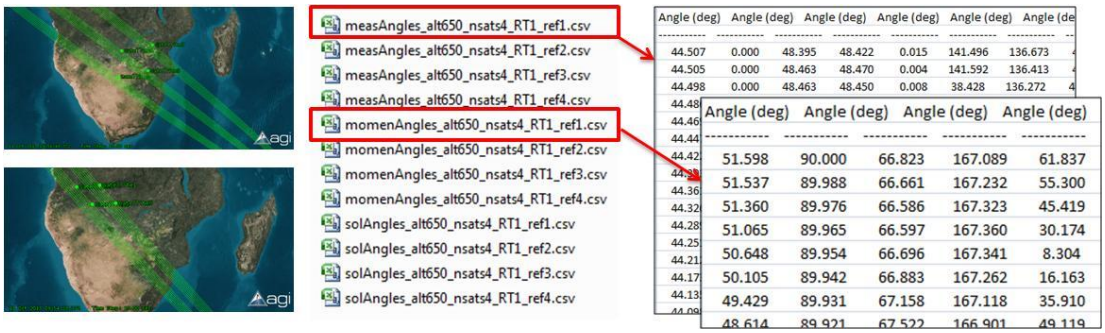

Figure 24: Process Flow for Angular Metric calculation in the LVLH frame using different formation flight architectures, pre-defined by design variables

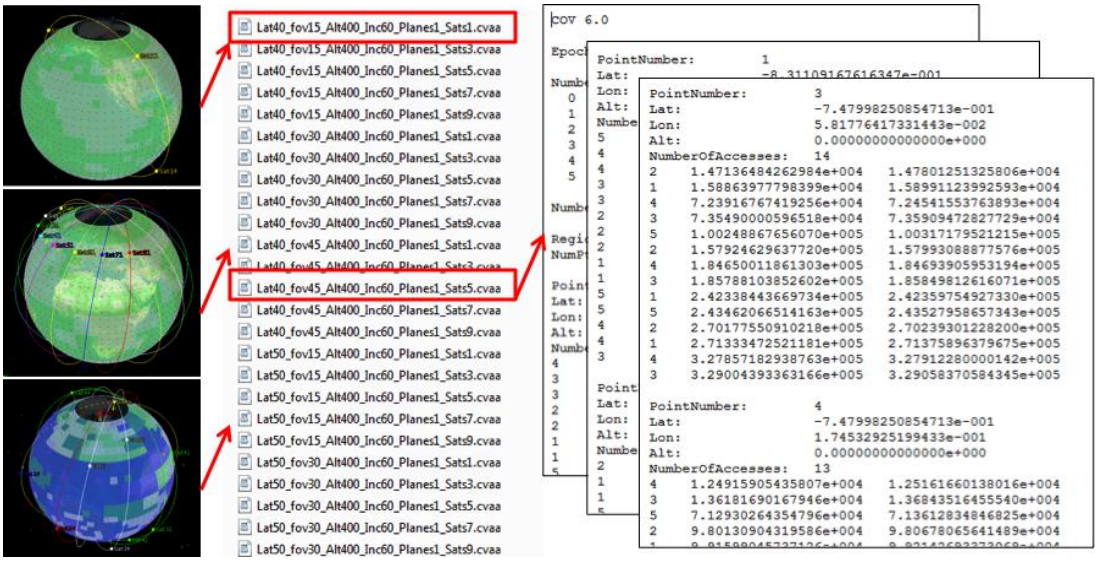

Figure 25: Process Flow for Temporal Metric calculation globally or specific areas or latitudes of interest (ECEF frame) using different constellation architectures, pre-defined by design variables.

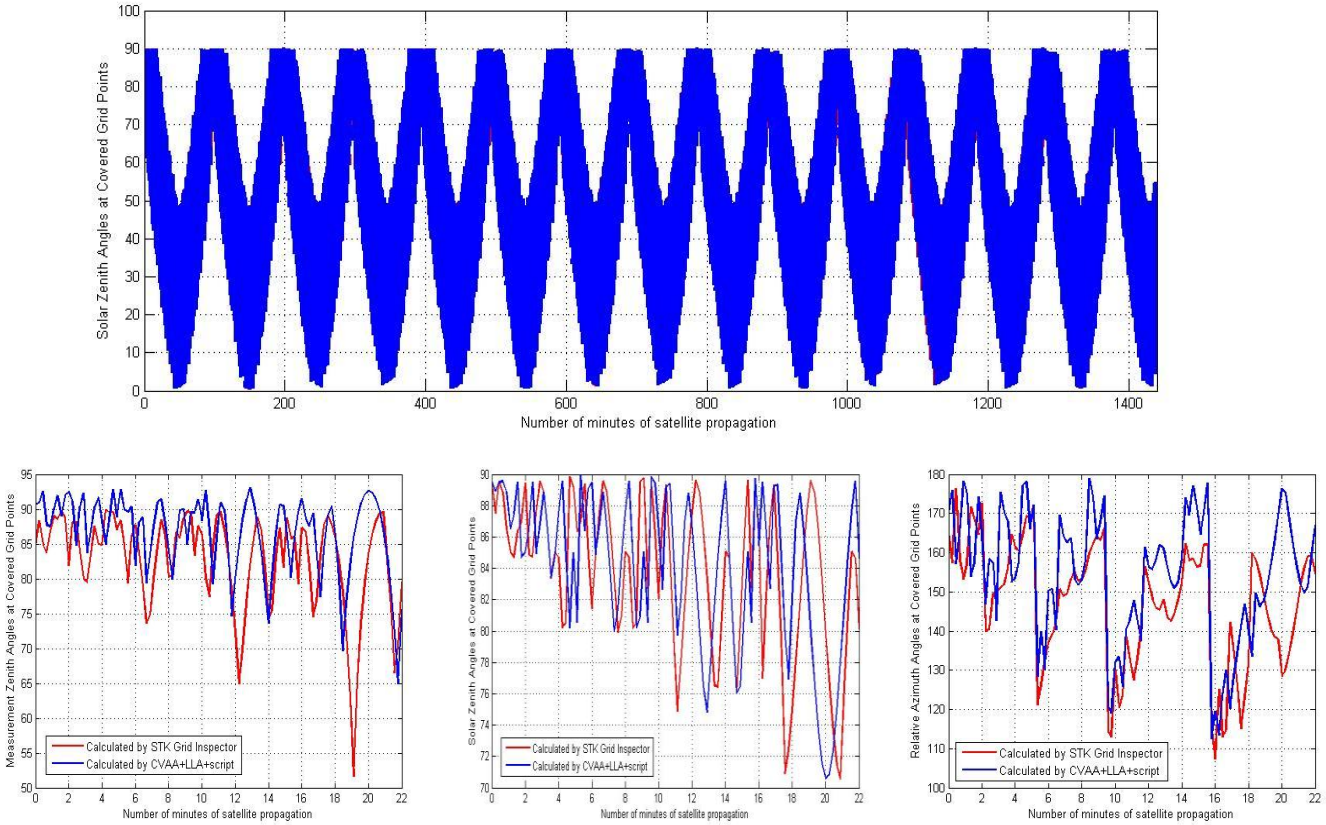

Figure 26: Validation of the VZA, SZA, and RAZ calculated by the proposed tool (blue) at every grid point and time instant those calculated by STK-GI (red). The top panel shows one angle as seen by a single satellite at every minute for a day while the bottom panels show all three angles over a 22 minute period, for better visualization. Average error <5 deg is negligible for a grid resolution of 5 deg, time resolution of 1 min, satellite ground velocity of 7.3 km/s.

The reports are named as before, however with different design variables. For example, the first one is a 1 plane, 1 satellite design at a 400 km altitude/ 60 deg inclination, a 15 deg instrument field of view for latitude coverage below 40 deg. Each access report is a detailed text file - Figure 25 third column - containing the time period (from when to when) at which every grid point is accessed by every sensor. These .cvaa files (per architecture) are post-processed to provide customized temporal metrics such as revisit time, time for first access, number of accesses, time for global coverage, etc. for every grid point and the globe. Science metrics dependent on such temporal metrics can easily be

calculated by plugging in the science evaluation module, modeled after an OSSE. Since the analysis is global and over mission lifetime, the metrics calculated are spatial and temporal. A separate script is also available for analyzing specific grid points in the same way as above, thus saving the computational resources required for full global analysis. For any target location or ground station, a text access report is automatically generated by MATLAB-commanded STK and automatically repeated for multiple architectures. Each generates an access report, which can be post-processed to generate customized metrics as described above.

STK, without the parallel processing license and dozens of available cores, was found to be inefficient for architecture studies using customized angular metrics. For example, the following angles are required to be calculated at every grid point and time instant for every architecture: MZA for each satellite (angle between the satellite vector at the ground spot and the zenith; <90 deg), SZA (angle between the sun vector at the ground spot and the zenith; <90 deg for solar spectrum) and RAZ (angle on the horizontal between the satellite vector projection and sun vector projection at the ground spot; <360 deg). The number of calculated angles is the product of the number of ground points (1651 by default), number of satellites, number of angles (3 by default), number of architectures and number of time steps. STK calculates all of them using a tool called Grid Inspector which loops over the number of points, satellites and angles, and re-calculates access for all loops, therefore taking 5 days to compute only 1 angle for a 64 satellite constellation.

To improve efficiency, our tool uses STK only for temporal and spatial analysis, and contains a standalone module for customized metric calculations such as angular outputs. The algorithm is as follows: (1) The High Precision Orbit Propagator (HPOP) using the Jacchia-Roberts Atmospheric Model with up to J4 terms is used to propagate the all satellite orbits in every architecture and the resultant states per time step saved as text files. (2) The access reports for all architectures – as seen in Figure 25 - are saved for exact global coverage. (3) The grid point information is saved. The above three outputs from STK are then post-processed to calculate the required hundreds of thousands of angles offline. The results are validated against those calculated by STK's Grid Inspector for one satellite propagated over one day. A reasonably good fit is seen for all grid points and all times with less than 5 deg. of average error. This error is less than half the angular resolution available by a grid and time resolution of 5 deg. and 1 min, for a satellite ground velocity of 7.3 km/s, hence considered negligible. All sampled angles, their dependent metrics or any other customized metrics dependent on global or temporal coverage, will be calculated in the above way. The orbits in our study are limited to LEO (the tool is unrestrictive). All other variables are set based on the case study. For example, in an ERB application, an FOV of 130 deg and a maximum of 64 satellites were simulated[12].

8. SELECTED RESULTS FROM CASE STUDIES

The analysis framework described is used to streamline the design variables, followed by the formation or constellation architecture generation software used to generate thousands of relevant designs for multi-angular observation. This section shows the angular and temporal outputs for some architectures, to demonstrate the utility of the tool in making decisions after considering conflicting objectives of performance. The objectives can be extended to spatial, and spectral sampling, and also cost.

Formation Flight

Formations are used to increase sampling in the spatial and angular dimension. A 4-satellite formation with a circular chief orbit at 650 km, 51.6deg inclination is considered, corresponding to an easily available secondary payload launch. If the 3 non-chief satellites were to have one of the differential RAAN-TA slots in Table 1, 56 architectures are possible. The angular outputs (VZA, RAZ only) of two of those architectures are plotted in Figure 27 and Figure 28. The TAAN-TA combinations are mentioned in the legend. A 4-hour simulation in LVLH allows for >2 orbits and all-biome sampling. For formation maintenance analysis, >1 year simulations are required.

The black lines correspond to MISR's 9 cameras. The MISR instrument is onboard the TERRA monolithic spacecraft. Since it has 4 forward and back cameras at the same boresight angle, there are four, unique and constant VZA and two RAZ. For any relative orbit architecture, any of the satellites could act as a reference and point straight down while the others point to the spot below it. The colors in Figure 27/25 represent the VZA and RAZ of each satellite in the cluster when a different one acts as reference. Figure 27/25-top does not show 4 VZA curves per color because of overlaps due to symmetry in differential Keplerian elements. For example, the VZA curve for sat#3 with sat#1 as reference (one of the blue curves) will be the same as the VZA curve for sat#1 with sat#3 as reference (one of the cyan curves). Moreover, if the differential RAAN and TA of 2 satellites are symmetric, for example Sat#3 and #4 in Figure 28, it results in more overlaps.

The solar zenith (SZA) for all architectures is nearly the same, because the satellites are fairly close and traverse nearly the same ground track with respect to the sun in the sky. The solar azimuth is very different, which contributes to the very complex RAZ plots. Obviously, it is quantitatively impossible to judge the better architecture among the Figure 27/25 (or thousands more) looking at (2N+1) angle curves per architecture and N-times more if different reference satellites are considered. While polar plots (Figure 27-bottom panels) offer better representation of the angular spread at any instant of time, each N-sat architecture has N of these spreads for every time instant and solar zenith. The panels also show how different the spread is when a different reference is used for the same architecture. The only way to evaluate these angular spreads is thus to feed them into an OSSE which calculates the

BRDF-error (or error in relevant products like albedo) per time step. The coupled MBSE+OSSE model is thus an indispensable judge to distinguish architectures based on science performance of their angular sampling.While NFOV formation angular outputs can be analyzed in the LVLH frame above, the WFOV angular outputs are best analyzed in the ECEF frame using constellation software.

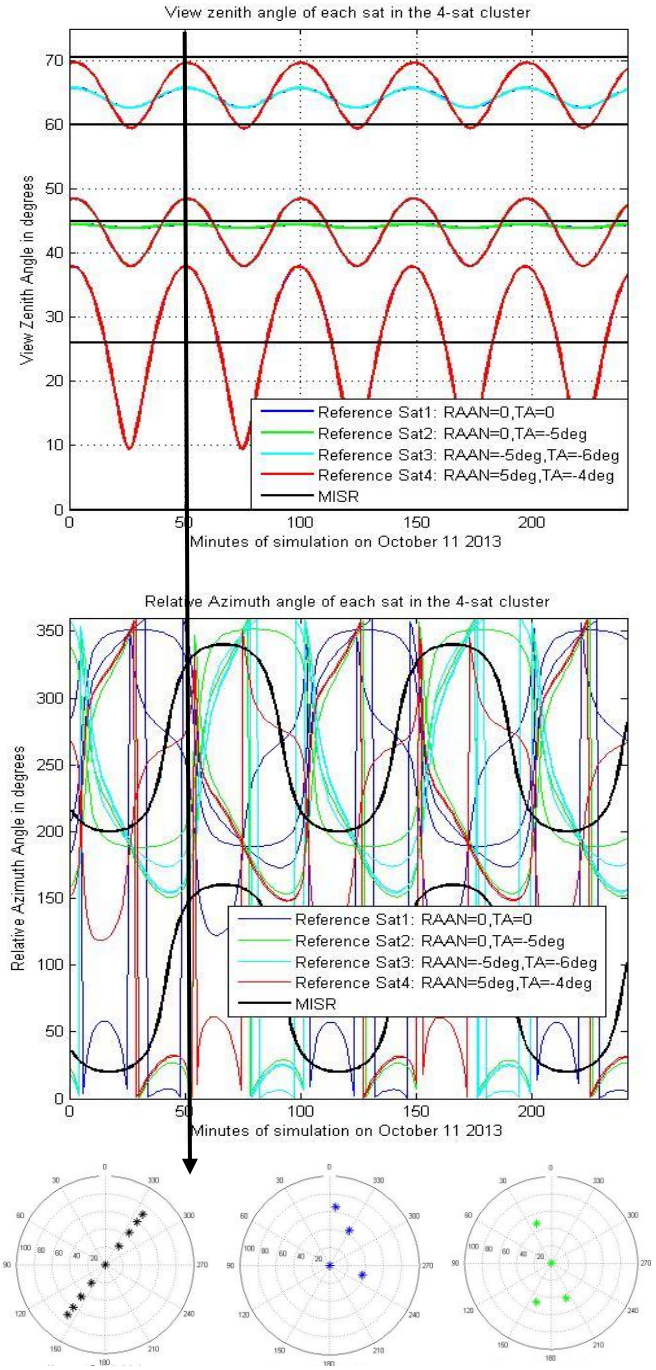

Figure 27: View zenith angle (top) and relative azimuth wrt Sun (bottom) of every satellite in a 4-satellite cluster in configured as one architecture – legend - when each is used as reference (grouped by color) and MISR (black). Bottom panels show the VZA-RAZ spread on a polar plot for t=50min for MISR (black) and cluster with Sat#1 (blue) and #3 (green) as reference.

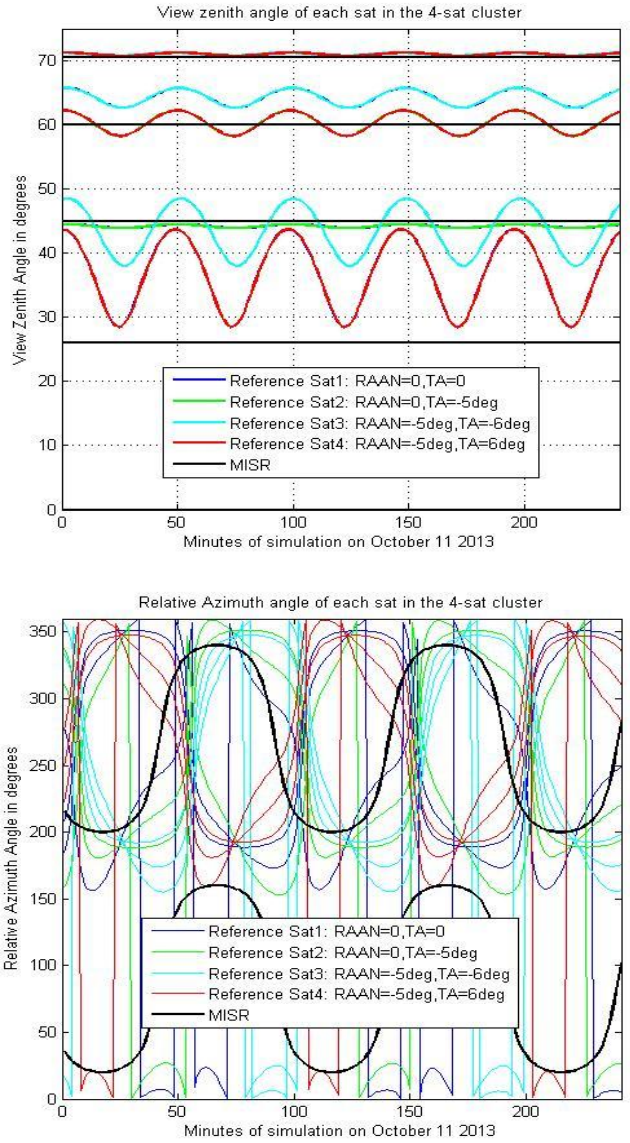

Figure 28: View zenith angle (top) and relative azimuth wrt Sun (bottom) of every satellite in a 4-satellite cluster configured in another architecture when each is used as reference (grouped by color) and MISR (black).

Constellations

Constellations to improve angular sampling has been demonstrated in Reference[12] and shown in Figure 1-right. Constellations of individual satellites or clusters (clustellations) improve sampling in the temporal dimension. A Walker constellation with varying number of satellites and FOVs were simulated for a constant altitude of 709 km and inclination of 98.18 deg., in keeping with the orbit of the A-Train and EOS satellites. Plane-Sat arrangement was not considered because it does not affect revisit time as long as uniformly arranged. Only latitudes below 70 deg. were considered. Figure 29 shows the maximum revisit time provided by all the architectures. A monolithic spacecraft with 15 deg FOV (e.g. Landsat) provides a 350 hour revisit – black circle on Figure 29's left

and full global map on Figure 29's right top. The results show that at least 14 such satellites are required for a daily revisit (Figure 29 black line) and 16 satellites for a daily repeat (analytical calculation). Doubling the FOV to 30 deg allows the same revisit in about quarter the satellites (4 satellites). The right panel also shows that revisits are far more frequent at higher latitudes than lower ones for polar constellations.

While revisit time does not depend on constellation arrangement, metrics such as time required for full global coverage does. Figure 30 shows the time taken for the last grid point on the globe is accessed by different constellation architectures. The results from our tool show that global coverage is faster if the same number of satellites is arranged in more planes. In fact, lesser number of satellites (e.g. 8 satellites in red vs. 12 satellites in grey) can achieve coverage faster if arranged in more planes. The trade-off however is in terms of cost because launching into 8 planes requires 7 plane changes (each costing a bulk of fuel) or needs 8 times the number of launches than launching into 1 plane. The increased performance and cost saved in developing 4 extra satellites can be compared against the cost of launching into 8 instead of 1 plane for the optimal design decision.

The 8 satellite arrangement can be further analyzed by plotting the timeline of global access (until 100% is accessed) - Figure 31(bottom). Walker Delta arrangements are seen to be better than Walker Star in time to global access and all curves are compared to the monolithic counterpart in the same orbit. The monolithic spacecraft takes 14 days for full global access as seen earlier and is shown with a black line, called 'Landsat' because it is an existing spacecraft in the same orbit with a 16-day repeat cycle. Figure 31's curves are very useful in deciding which design to choose depending on the integration time available over measurements and the coverage flexibility. For example, if a 2 day integration time is available, then the 8 plane constellation is equivalent to having continuous global coverage and there is no value in adding more satellites. Better angular output using WFOV sensor constellations and its utility in reducing uncertainties in the Earth's Radiation Budget has also been demonstrated using this tool[12]. It can be used to select a design, given a required temporal resolution, spatial or angular coverage.

There are many other constellation types that can be analyzed using similar metrics and associated OSSEs, which can be incorporated into the presented software tool. Moreover, as many secondary payload launch opportunities become available, multiple satellites be flown piggy-back on subsequent launches with very different orbital parameters. The presented tool can help answer important questions about the performance trade-offs associated with such ad-hoc constellations[41], especially with regard to science trade-offs.

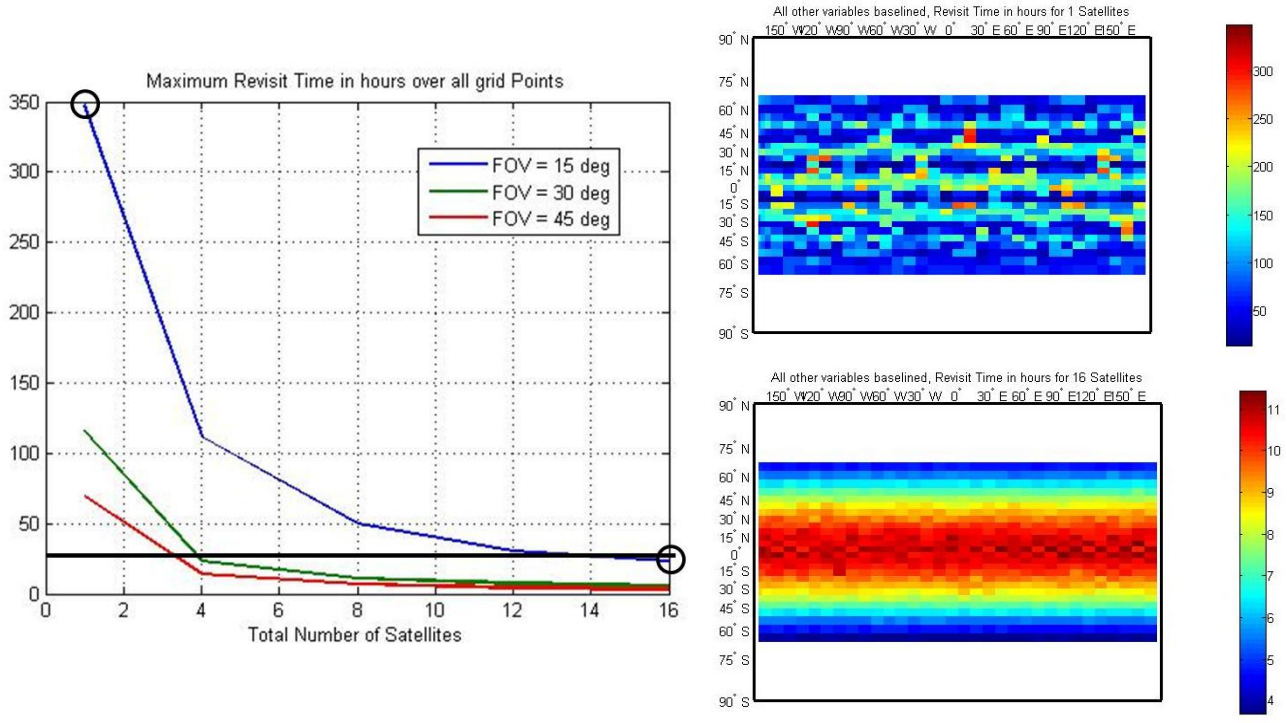

Figure 29: Results from our temporal trade tool using Revisit time as a metric. [Left] Maximum revisit time over all grid points as a function of payload FOV and number of satellites in a Walker constellation at 709 km altitude, 98.18 deg inclination. The thick black line indicates at least a 24 hour revisit for any point and the black circles indicate the designs for which global revisit time is shown on the right. [Right] Average revisit time at every grid point, calculated over a 16 day period, for a 1 (top) and 16 (bottom) satellite constellation.

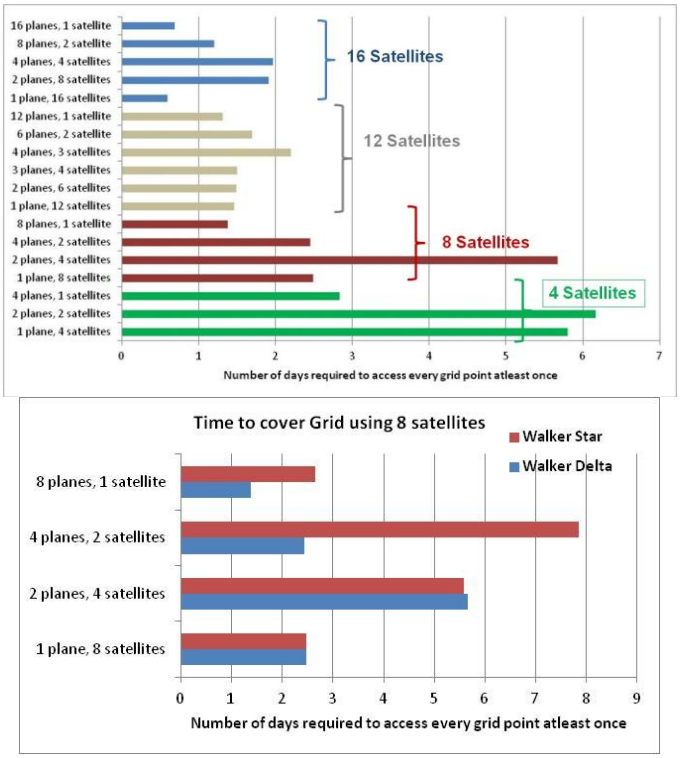

Figure 30: Time required to global coverage for Walker constellations (at 709 km, 98.18 deg) with varying number of satellites and their planar arrangement. Walker Delta constellations, on an average, show lesser time than Walker Star.

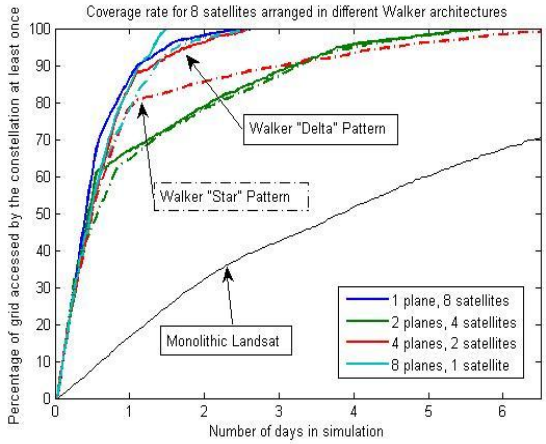

Figure 31: Percentage of the globe covered with respect to time for Walker constellations (at 709 km, 98.18 deg) with 8 satellites arranged in different planes (colors) and in Delta (continuous line) or Star (dotted line) arrangements.

9. SUMMARY AND FUTURE WORK

This paper identifies a lack in open-source, orbital analysis software for understanding the complex design trades for distributed space missions (DSM), both constellations and more pertinently formation flight. A gap in the measurement making abilities of monolithic spacecraft in the field of multi-angular earth observation is also identified and DSMs proposed to fill this gap. BRDF and its dependent products, such as albedo and ERB, are assumed to be appropriate metrics for angular sampling on Earth (solar spectrum).

A framework and relevant software has been developed to analyze the full tradespace of LEO formations (in the LVLH frame over all Earth biomes) and constellations (in the ECEF frame) so that NFOV and WFOV sensors, respectively, can provide angular coverage of all/any point on Earth. All software is written on MATLAB, STK or Excel and is completely automated in terms of architecture generation and evaluation. The formation models are arranged in increasing order of fidelity and computational requirements, and serve as a method to streamline the design variables as the models get more complex. The highest fidelity models are coded in MATLAB-driven STK and can generate thousands of architectures permuted from the streamlined variables. The output per architecture is the angular spread for every LVLH point at every instant of time, which serves as inputs into a science evaluation model to determine how much the spread reduces BDRF uncertainties. The constellation software is capable of generating angular, spatial and temporal metrics, because the analysis is in the global, ECEF frame. As with formations, constellation architectures can be selected either by comparing the intermediate metrics like angular spread or revisit rate or by passing it into OSSEs to compare science-based uncertainties.

There is quantitative dependence between angular and temporal sampling (metrics in this paper) and spatial, spectral and radiometric resolution (introduced and not discussed). Previous studies have discussed this dependence for specific spectrometers and radiometers in the context of multi-angular remote sensing[7][12]. Future work includes integrating those tools with the ones mentioned here, for more exhaustive DSM tradespace software.

Further work on this topic will be directed toward improving the proposed framework and developing the software tool further than the shown preliminary version. Once complete, the tool is expected to be available as open-source software based on Python or Octave and will interface with GSFC's GMAT[47]. The constellation space will be expanded to more types and include heterogeneous and ad-hoc designs. Users will also be able to scale up formation clusters to more than one, where clusters will provide angular spread and the clustellation will provide frequent observations of that spread. The described tool has been applied to design and validate DSM architectures when coupled with OSSEs for BRDF[43], albedo[13], gross primary productivity[8] and ERB[12] estimation and can be extended to more studies in the future.

REFERENCES

[1] E. M. C. Kong and D. W. Miller, "Optimal spacecraft reorientation for earth orbiting clusters: applications to

Techsat 21," *Acta Astronaut.*, vol. 53, no. 11, pp. 863–877, Dec. 2003.
[2] S. Nag, C. K. Gatebe, and O. L. De Weck, "Relative Trajectories for Multi-Angular Earth Observation using Science Performance Optimization," in *IEEE Xplore, Aerospace Conference 2014*, Big Sky, Montana, 2014.
[3] B. Yost, "EDSN-Edison Demonstration for SmallSat Networks Overview," presented at the Small Satellite Conference, Logan, Utah, 2013.
[4] M. G. O'Neill, H. Yue, S. Nag, P. Grogan, O. de Weck, "Comparing and Optimizing the DARPA System F6 Program Value-Centric Design Methodologies," in *AIAA Space Conference*, Anaheim, California, 2010.
[5] Aleksandr A. Kerzhner, Michel D. Ingham, Mohammed O. Khan, Jaime Ramirez, Javier De Luis, Jeremy Hollman, Steven Arestie, and David Sternberg, "Architecting Cellularized Space Systems using Model-Based Design Exploration," in *AIAA SPACE 2013 Conference and Exposition*, 0 vols., American Institute of Aeronautics and Astronautics, 2013.
[6] K. T. Alfriend, S. R. Vadali, and H. Schaub, "Formation flying satellites: Control by an astrodynamicist," *Celest. Mech. Dyn. Astron.*, vol. 81, no. 1–2, pp. 57–62, 2001.
[7] S. Nag, K. Cahoy, O. de Weck, C. Gatebe, B. Pasquale, G. Georgiev, T. Hewagama, and S. Aslam, "Evaluation of Hyperspectral Snapshot Imagers onboard Nanosatellite Clusters for Multi-Angular Remote Sensing," in *AIAA Space Conference*, San Diego, 2013.
[8] S. Nag, C. K. Gatebe, T. Hilker, F. G. Hall, L. P. Dyrud, O. L. De Weck, "Gross Primary Productivity Estimation using Multi-Angular Measurements from Small Satellite Clusters," in *International Geoscience and Remote Sensing Symposium (IGARSS 2014)*, Quebec City, Canada, 2014.
[9] D. J. Diner, J. C. Beckert, et al, "Multi-angle Imaging SpectroRadiometer (MISR) instrument description and experiment overview," *Geosci. Remote Sens. IEEE Trans. On*, vol. 36, no. 4, pp. 1072–1087, 1998.
[10] X. Xiong, R. Wolfe, et al, "Terra and Aqua MODIS Design, Radiometry, and Geometry in Support of Land Remote Sensing," *Land Remote Sens. Glob. Environ. Change*, pp. 133–164, 2011.
[11] S. Nag, K. Cahoy, and O. L. De Weck, "Subsystem Support Feasibility for Formation Flight measuring Bi-Directional Reflectance," in *IEEE Xplore, Aerospace Conference 2015*, Big Sky, Montana, USA, 2015.
[12] S. Nag, "Satellite Constellation Mission Design using Model-Based Systems Engineering and Observing System Simulation Experiments," in *Proceedings of the Small Satellite Conference*, Logan, Utah, 2014.
[13] S. Nag, C. Gatebe, D. W. Miller, and O. L. De Weck, "Effect of Satellite Formation Architectures and Imaging Modes on Albedo Estimation of major Biomes," *Acta Astronaut.*, 2015.
[14] O. L. De Weck, U. Scialom, and A. Siddiqi, "Optimal reconfiguration of satellite constellations with the auction algorithm," *Acta Astronaut.*, vol. 62, no. 2, pp. 112–130, 2008.
[15] S. Nag, "Collaborative Competition for Crowdsourcing Spaceflight Software and STEM Education using SPHERES Zero Robotics," Dual S.M., Massachusetts Institute of Technology, Cambridge, Massachusetts, U.S.A., 2012.
[16] J. Esper, S. Neeck, W. Wiscombe, M. Ryschkewitsch, and J. Andary, "Leonardo-BRDF: A New Generation Satellite Constellation," presented at the International Astronautical Conference, Rio de Janeiro, Brazil, 2000.
[17] F. E. Nicodemus, *Geometrical considerations and nomenclature for reflectance*, vol. 160. US Department of Commerce, National Bureau of Standards Washington, D. C, 1977.
[18] A. Lyapustin, C. K. Gatebe, et al, "Analysis of snow bidirectional reflectance from ARCTAS Spring-2008 Campaign," *Atmos Chem Phys*, vol. 10, no. 9, pp. 4359–4375, 2010.
[19] S. Liang, *Advances in land remote sensing: System, modelling, inversion and application*. Springer, 2008.
[20] B. A. Wielicki and E. F. Harrison, "Mission to planet Earth: Role of clouds and radiation in climate," *Bull. Am. Meteorol. Soc.*, vol. 76, no. 11, 1995.
[21] S. C. Spangelo, et al, "Applying model based systems engineering (MBSE) to a standard CubeSat," in *Aerospace Conference, 2012 IEEE*, 2012, pp. 1–20.
[22] P. T. Grogan, "A flexible, modular approach to integrated space exploration campaign logistics modeling, simulation, and analysis," Massachusetts Institute of Technology, 2010.
[23] H. Heidt, J. Puig-Suari, et al, "CubeSat: A new generation of picosatellite for education and industry low-cost space experimentation," Small Satellite Conference, Logan, Utah, 2000.
[24] O. L. De Weck, R. D. Neufville, and M. Chaize, "Staged deployment of communications satellite constellations in low earth orbit," *J. Aerosp. Comput. Inf. Commun.*, vol. 1, no. 3, pp. 119–136, 2004.
[25] G. W. Hill, "Researches in the lunar theory," *Am. J. Math.*, vol. 1, no. 1, pp. 5–26, 1878.
[26] W. H. Clohessy, R.S. Wiltshire, "Terminal Guidance System for Satellite Rendezvous," *J. Aerosp. Sci.*, vol. 27, pp. 653–658, 1960.
[27] J. R. Wertz, *Orbit & Constellation Design & Management, second printing ed. El Segundo*. California: Microcosm Press, 2009.
[28] T. J. Lang and W. S. Adams, "A comparison of satellite constellations for continuous global coverage," in *Mission Design & Implementation of Satellite Constellations*, Springer, 1998, pp. 51–62.
[29] S. A. Schweighart, R. J. Sedwick, "High-Fidelity Linearized J Model for Satellite Formation Flight," *J. Guid. Control Dyn.*, vol. 25, no. 6,, 2002.
[30] M. Sabatini, G. B. Palmerini, "Linearized formation-flying dynamics in a perturbed orbital environment," in *Aerospace Conference, 2008 IEEE*, 2008, pp. 1–13.
[31] "Systems Tool Kit," *Analytical Graphics Inc.* [Online]. http://www.agi.com/products/stk/modules/default.aspx/id/stk-free. [Accessed: 04-Mar-2013].

[32] H. Schaub, "Spacecraft relative orbit geometry description through orbit element differences," in *14th US National Congress of Theoretical and Applied Mechanics, Blacksburg, VA*, 2002.
[33] S. W. Paek, "Reconfigurable satellite constellations for geo-spatially adaptive Earth observation missions," Massachusetts Institute of Technology, 2012.
[34] R. Legge, "Optimization and Evaluation of Reconfigurable Satellite Constellations Under Uncertainty," Massachusetts Institute of Technology, 2014.
[35] T. J. Lang, "Walker constellations to minimize revisit time in low earth orbit.," *Adv. Astronaut. Sci.*, vol. 114, p. 16, 2003.
[36] J. R. Wertz, D. F. Everett, and J. J. Puschell, *Space Mission Engineering:The New SMAD*, First. Microcosm Press, 2011.
[37] D. Mortari, M. P. Wilkins, and C. Bruccolerr, "The flower constellations.," *Adv. Astronaut. Sci.*, vol. 115, pp. 269–290, 2003.
[38] M. P. Wilkins, C. Bruccoleri, and D. Mortari, "Constellation Design Using Flower Constellations," *Pap. AAS*, pp. 04–208, 2004.
[39] M. P. Wilkins and D. Mortari, "Constellation Design via Projection of an Arbitrary Shape onto a Flower Constellation Surface," in *Paper of the 2004 AIAA/AAS Astrodynamics Specialist Conference, Providence, Rhode Island*, 2004.
[40] M. E. Avendano and D. Mortari, "New Insights on Flower Constellations Theory," *Aerosp. Electron. Syst. IEEE Trans. On*, vol. 48, no. 2, pp. 1018–1030, 2012.
[41] A. Marinan, A. Nicholas, K. Cahoy, "Ad hoc CubeSat constellations: Secondary launch coverage and distribution," *IEEE Aerospace Conference*, 2013,.
[42] S. Nag, J. LeMoigne, and O. L. De Weck, "Cost and Risk Analysis of Small Satellite Constellations for Earth Observation," in *IEEE Xplore, Aerospace Conference 2014*, Big Sky, Montana, USA, 2014.
[43] S. Nag, C. K. Gatebe, and O. L. De Weck, "Observing System Simulations for Small Satellite Clusters estimating Bi-Directional Reflectance," *Int. J. Appl. Earth Obs. Geoinformation*, 2015.
[44] M. D. King, M. Strange, P. Leone, L. Blaine, "Multiwavelength scanning radiometer for airborne measurements of scattered radiation within clouds," *J. Atmospheric Ocean. Technol.*, vol. 3, pp. 513–522, 1986.
[45] C. K. Gatebe, "Airborne spectral measurements of surface–atmosphere anisotropy for several surfaces and ecosystems over southern Africa," *J. Geophys. Res.*, vol. 108, no. D13, 2003.
[46] S. Nag, J. LeMoigne, D. W. Miller, and O. L. De Weck, "A Framework for Orbital Performance Evaluation in Distributed Space Missions for Earth Observation," in *IEEE Xplore, Aerospace Conference 2015*, Big Sky, Montana, USA, 2015.
[47] S. P. Hughes, "General Mission Analysis Tool (GMAT)," 2007.

BIOGRAPHIES

Sreeja Nag *is a PhD candidate in Space Systems Engineering at the Massachusetts Institute of Technology and a part-time research engineer at NASA Ames Research Center. She has a dual SM in Aeronautics & Astronautics Engineering along with Technology & She has worked at NASA Goddard Space Flight Center, has summer research experience with NASA JPL in 2008, the European Space Agency (ESTEC) in 2010 and led the SPHERES Zero Robotics Program in 2011. Email: sreeja_n@mit.edu*

Jacqueline Le Moigne *is the Assistant Chief for Technology in the Software Engineering Division at NASA Goddard where she is currently leading a study on Distributed Spacecraft Missions. She has performed extensive work in developing new technologies for remote sensing data analysis, e.g., image registration, high-performance and onboard processing. She has published over 100 publications and recently co-edited a book on "Image Registration for Remote Sensing." Email: Jacqueline.LeMoigne@nasa.gov*

David W. Miller *is a Hunsacker Professor of Aeronautics and Astronautics at the Massachusetts Institute of Technology. He is currently serving as the Chief Technologist at NASA Headquarters. As the Director of the Space Systems Laboratory at MIT, he was the PI of the SPHERES program aboard the International Space Station and, more recently, served as the vice chair of the Air Force Scientific Advisory Board. Email: millerd@mit.edu*

Olivier de Weck *is a Professor of Aeronautics and Astronautics and Engineering Systems at the Massachusetts Institute of Technology. He is also the Executive Director of MIT Production in the Innovation Economy (PIE) Study and the Co-Director, Center for Complex Engineering Systems at KACST and MIT. Email: deweck@mit.edu*